buildings

MDPI

Article

Experimental and Finite Element Study on the Sliding Friction Isolation System of Multi-Story Modular Container Building Structure

Yang Zuo [1,*] and Xiaoxiong Zha [2]

[1] School of Environment and Civil Engineering, Dongguan University of Technology, Building 12M202-2, Songshan Lake, Dongguan 523808, China
[2] School of Intelligent Civil and Ocean Engineering, Harbin Institute of Technology, Building E332, Nanshan District, Shenzhen 518055, China
* Correspondence: zuoyang@dgut.edu.cn

Abstract

Given the widespread application of multi-story modular container building structures, this article proposes a new seismic isolation system called the "sliding friction isolation system (IS)" that utilizes friction energy dissipation between containers. Firstly, lateral stiffness tests were conducted on a 20 ft container, a 40 ft container, and 20 ft connected containers. The constraint consists of four fixed-bottom corner pieces, and the load is achieved using a symmetrical longitudinal concentrated loading method. Their stiffness values were 58.07 kN/mm, 33.41 kN/mm, and 60.03 kN/mm, respectively, providing the necessary parameters for IS. Secondly, an IS model was established, and based on the theory of random vibration, the relationship between c_{ei} (the equivalent damping of i layer of the structure) and μ (the inter-layer friction coefficient) of the system was obtained. Thirdly, a nonlinear finite element model of a six-story container building was established. Namely, the non-isolation system with standard damping ratios (NIS-sdr), the non-isolation system with equivalent damping ratio (NIS-edr), and the IS. Elastic-plastic nonlinear time-history analyses were then conducted to study the dynamic responses of three systems under strong earthquakes. The analyses yielded the top displacement of the structure, each structural layer's maximum displacement and displacement angle, the slip of each layer, the hysteresis loops, and the cumulative dissipated energy of IS. The results show that compared to NIS sdr and NIS edr, IS can effectively reduce the maximum interlayer displacement. The largest angular displacement between the structural layer of IS and NIS-edr is far less than that of NIS-sdr. The spectral characteristics of seismic waves (the EL-Centro wave, Taft wave, and artificial wave) can significantly affect the dynamic response of IS. Additionally, the length of the sliding hole on the corner piece can be set to 35 mm based on the displacement of each layer under the Taft wave to meet the standards for container houses (T/CECS 1932-2025).

Keywords: modular building seismic performance; multi-story container structure; container stiffness; connected containers; sliding friction isolation system; equivalent damping ratio; numerical dynamic response

Check for updates

Academic Editor: Giuseppina Uva

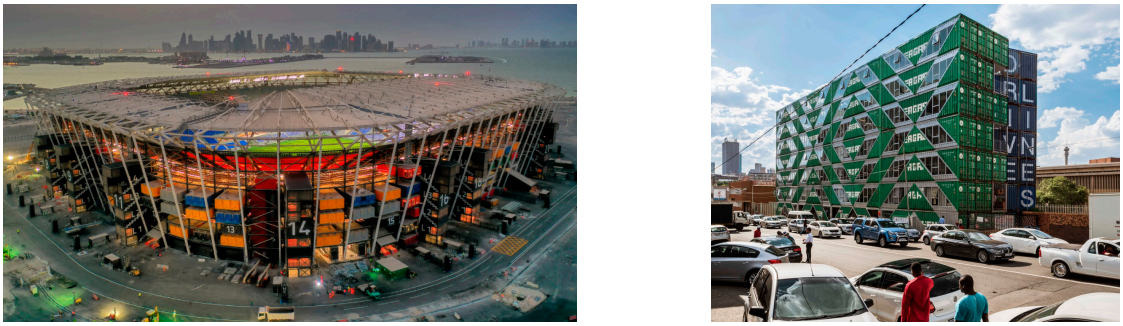
Received: 29 April 2026
Revised: 3 June 2026
Accepted: 18 June 2026
Published: 24 June 2026

Copyright: © 2026 by the authors. Licensee MDPI, Basel, Switzerland. This article is an open access article distributed under the terms and conditions of the Creative Commons Attribution (CC BY) license.

1. Introduction

1.1. Multi-Story Container Buildings and Their Advantages

Multi-story container buildings, as a lightweight and environmentally friendly modular steel structure, are increasingly used in residential and temporary housing, commercial and consumer spaces, public services and community building, industrial and office needs, special industries and technology integration applications, urban renewal and rural revitalization, post-disaster reconstruction, and other projects, as shown in Figure 1 [1,2].



(**a**) (**b**)

Figure 1. Multi-story container buildings. (**a**) 974 Stadium in Qatar; (**b**) Drivelines studios apartment building in South Africa.

Compared to traditional buildings, modular container buildings adopt an industrialized approach of "factory prefabrication + on-site assembly", significantly reducing construction cycles and resource consumption. Container construction has the following core advantages: extremely fast construction speed, shortened construction period by 40–80%; green and low-carbon, with outstanding environmental performance; more stable quality and high industrial standards; strong flexibility and scalability; small construction interference, suitable for densely populated urban areas; simplified approval and faster implementation. The construction cost has the characteristics of high material cost (50–60%), significantly reduced labor cost (30–40%), and additional transportation and lifting costs. Its total cost can be reduced by more than 30% compared to traditional buildings, and cost control is better.

The core differences between modular container building structures in traditional and modern applications are reflected in four aspects: functional positioning (from emergency use to urban integration), structural system (from simple stacking to system engineering), technology integration (from basic configuration to intelligent living), and policies and regulations (from temporary permits to legal compliance). The traditional model focuses on "rapid deployment and temporary turnover", while the modern model has evolved toward "permanent residence and urban landmarks", achieving a leap from functional to quality-oriented. The design and use of containers as building modules must meet various requirements, such as mechanical structural safety, building function adaptation, green energy conservation and environmental compliance, compliance with fire and corrosion prevention requirements, and complete land approval procedures. In addition, although containers as building modules have advantages such as flexibility and environmental protection, they still face various limitations in practical applications, such as flexibility of building space, comfort of living, safety of use, durability of structural steel, transportation and installation, laws and policies, etc.

In recent years, research on modular container buildings has mainly focused on architectural design, energy conservation, building structure optimization, environmental protection, thermal insulation, and production manufacturing [3–12]. On special occasions,

such as infectious disease hospitals, temporary camps, high-altitude areas, etc., relevant regulatory standards have also been introduced [13–15].

1.2. Progress in Modular Container Buildings Research

In terms of building structural performance and safety, Zha [16–18] provided a comprehensive investigation into the mechanical behavior of container structures under various conditions. The article employed the finite element method to analyze the performance of container structures under both normal and high-temperature conditions, highlighting the effects of thermal loading on structural integrity. The article focused on the in-plane stiffness of integrated container structures without openings, combining theoretical derivations with experimental validations to establish a reliable stiffness model. This article extended this work by examining container structures with holes, investigating how openings influence in-plane stiffness through similar theoretical and experimental methods. Collectively, these studies offered valuable insights and practical guidance for the safety assessment, damage prevention, and optimal design of container structures in engineering applications. Dan Adrian [19] proposed a novel inter-module connection method using customized corner fittings, high-damping rubber cores, and shape memory alloy bolts. Research has shown that the proposed inter-module connection exhibits good cyclic performance during lateral loading in the deformation mode of high-rise self-supporting modular building systems. Due to the effective contribution of each component to the combined mixed response, this connection successfully prevented significant plastic damage to the corner fittings. Wang [20] uses the optimality criterion to reduce the self-weight of prefabricated buildings while maintaining their overall stiffness. This study involves a three-story modular building with hinged joints and a frame structure with two different beam stiffnesses for the beam-column connection. The size optimization of the two structural systems was achieved through a numerically stable iterative OC algorithm. The proposed method can save a significant amount of steel for modular building systems without affecting modal stiffness. Lyu [21] analyzed the bending behavior of simple splice connections used for angle-supported steel modular buildings. The study found that the proposed connection has good ductility during the bending process. In the second stage, the applied load will continuously increase with the deformation of the specimen, indicating that the proposed connection has sufficient bending resistance reserve under large deformation conditions. Based on the farthest point method, a transition point is defined in the relationship between bending moment and connection angle, which has an important value for practical design. Lyu [22] analyzed in detail the mechanical behavior of splicing connections during vertical load transfer in full-size modular buildings. The results indicate that the proposed splicing connection did not cause any adverse phenomena before the overall buckling of the module column. During the loading process, splicing connections manifest in three stages. In the first stage, the involvement of splicing connections can be ignored. In the second stage, the joint provides constraints for the second-order bending moment at the bottom of the column. In the third stage, local deformation and gaps were discovered. Liew [23] introduced the progress of modular structures, with a focus on steel and concrete modular systems. He emphasized the constructability and robustness of these systems, with steel modular systems utilizing lightweight characteristics to achieve rapid assembly and structural integrity through corner support systems, while concrete modular systems prioritize the durability and fire resistance of composite structural wall systems. The lightweight steel-concrete composite system integrates the advantages of these two materials, providing longer spans, durability, and flexibility. Pejman [24] introduced a framework for constructing prefabricated multi-story buildings, whose pillars are a new type of swing steel that can be quickly assembled and disassembled. Research has shown that this design provides flexible space

for modular frame buildings, eliminates the requirement for structural cores, improves construction efficiency, and allows the backbone to use self-supporting units to support the building. This framework accelerates construction progress, reduces material consumption, and achieves high rigidity and reliable construction.

In the field of seismic resistance in container buildings, Zhang [25] conducted research on the collapse behavior of modular structures. A semi-rigid connection was selected for the current specimen to conduct vertical loading tests with internal column losses. The sample was found to have failed due to the breakage of beam-column connections within the module, with the floor beam breaking prematurely and the ceiling beam subsequently breaking. Throughout the entire loading process, the load-transfer mechanism and resistance contribution of the double-beam system were thoroughly analyzed. William [26] applied the newly proposed model to modular steel structures and studied the response of modular connections to simulated time-varying wind loads and seismic ground accelerations of the entire building. The building performance of two different connection methods was compared, and it was shown that the new simplified model is very suitable for numerical simulation. The analytical basis of the model enables it to be applied to different connection geometries, which helps to better reflect the building response. Zhang [27] studied the collapse of steel module buildings affected by angular modulus loss. The results showed that the load-displacement curve presented three stages, with the maximum load being about 1.6 times its yield load. The final failure mode was the fracture of the flange bolts at the module connection, significant separation of the double-layer beam interface, and relative displacement exceeding 50 mm. The top module beam was in a compressed state, and the bottom beam was in a tensile state. The maximum axial force could reach 600 kN, which was 3/4 of the yield axial load of the beam. Zha [28,29] investigated the mechanical performance of container structures under different loading conditions. The article analyzed the seismic behavior of container structures, examining their response and durability during earthquake actions to support seismic design. The article focused on multi-body container buildings, presenting theoretical and finite element studies on longitudinal stiffness. Together, these works contributed to understanding container structural behavior under both dynamic seismic loads and static stiffness requirements, providing valuable references for safe and efficient container-based construction. Ze [30] proposed an air spring lead rubber bearing seismic isolation device. An analysis was conducted on a four-story three-span building using it, and the results showed that it effectively reduced seismic effects. The horizontal peak acceleration, column shear force, and node displacement angle were significantly reduced. By optimizing the target period ratio and transmission ratio, the isolation performance of the building can be improved. It is recommended that the target isolation period be at least 1.75, combined with a lower vertical transmission ratio, to achieve the best results. Ze [31] introduced air spring lead rubber bearings and proposed a design method based on seismic isolation devices in accordance with Chinese standards. This method mainly considers the target period ratio and design transmission ratio, and designs a four-story three-span structure to analyze its seismic isolation performance, in order to determine the target period ratio and design transmission ratio under different seismic performance targets. The results show that this calculation method can accurately obtain the parameters of air spring lead rubber bearings and achieve the expected goals.

1.3. The Seismic Challenge of Multi-Story Container Buildings

Modular container buildings have been widely deployed in regions with significant seismic hazards, as shown in Figure 2, including the Pacific Rim (Japan, China, Chile, New Zealand) where peak ground accelerations (PGA) can exceed 0.4 g during rare earthquakes, the Mediterranean (Italy, Greece, Turkey) with design PGAs of 0.2–0.35 g, and even moderate-

seismicity areas such as South Africa. According to the Global Seismic Hazard Assessment Program (GSHAP), approximately 30% of the world's population lives in areas with PGA > 0.2 g (10% exceedance probability in 50 years). Despite this widespread deployment in seismically active zones, the seismic performance of multi-story modular container buildings remains a critical concern. Unlike conventional steel structures, container buildings exhibit several adverse seismic responses due to their unique characteristics: low inherent damping (2–3% vs. 5% for conventional steel), slow vibration attenuation, vulnerable inter-module connections susceptible to uplift and slippage, and the "whipping effect" caused by low lateral stiffness of longer containers (e.g., 40 ft). Field observations from past earthquakes have confirmed severe damage to inadequately anchored modular structures, including corner fitting rupture, sidewall buckling, and stack overturning.

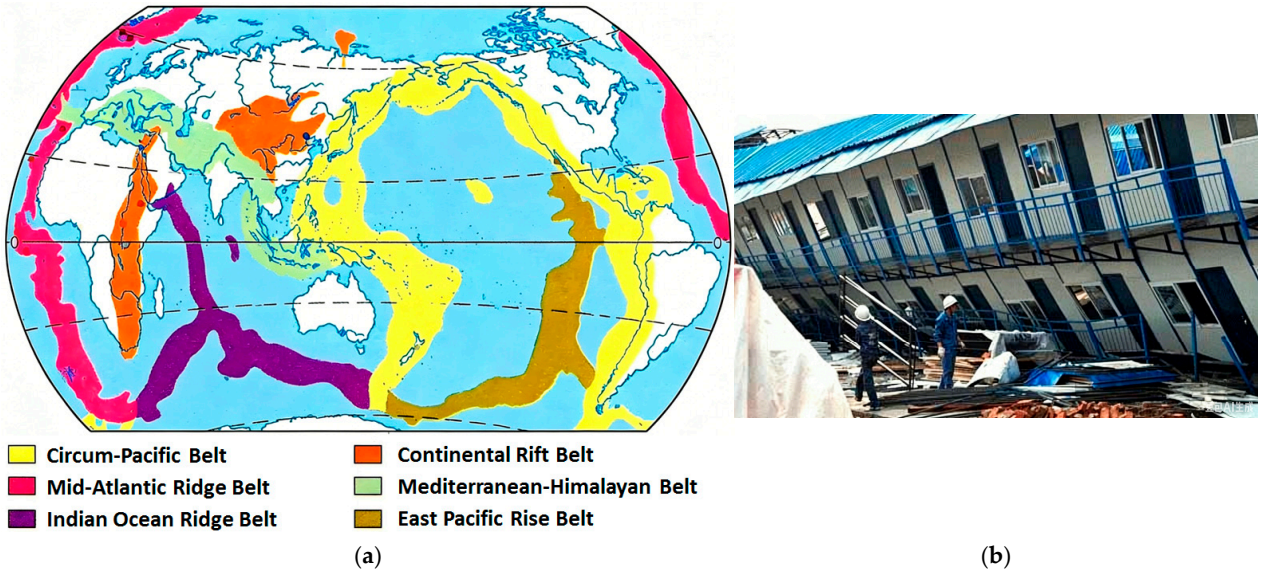
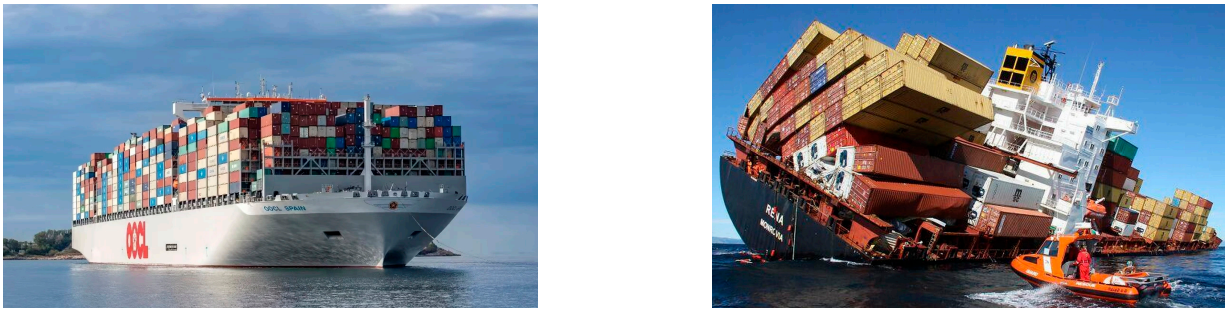


Figure 2. Seismic challenge of modular buildings. (**a**) World earthquake disaster zone; (**b**) Modular building collapse.

The seismic resistance of modular multi-layer container buildings is similar to the dynamic response of containers stacked on shipping ships in waves, as shown in Figure 3 [32,33]. Both need to deal with complex lateral and longitudinal impact forces. Although the excitation sources are different—earthquakes are crustal movements and waves are fluid dynamics—their mechanical effects on multi-layer stacked containers are highly similar. The shipping industry has developed a mature system to solve this problem, such as optimizing loading and unloading efficiency and space utilization through vertical stacking, preventing container displacement through the use of grid-style cargo racks, and controlling the center of gravity of ships by adjusting the weight of ballast water. Many principles of maritime transportation have been applied to container construction. For example, drawing on the principle of container anchoring, seismic wave energy is absorbed through horizontal and vertical shock-absorption mechanisms, combined with plug-in rapid connection fixation, effectively reducing relative displacement between containers and maintaining overall stability of container construction at the epicenter. For example, by strengthening the main components and nodes, the seismic resistance of an 8-degree earthquake crack has been achieved, which is equivalent to resisting the impact of a 6.4 magnitude earthquake, effectively reducing the "whip effect" problem of top containers. In addition, a multi-layer container load monitoring system is equipped to provide real-time feedback on multi-layer stacking stress, tilt angle, and other data, enhancing emergency response capabilities.



(**a**) (**b**)

Figure 3. Container ship. (**a**) Container ship operating normally; (**b**) Container cargo collapses.

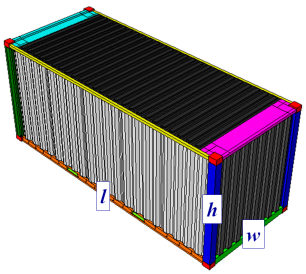
Therefore, the research objective of this article is to analyze and verify the seismic isolation effect of IS based on the widely used modular container building structure. By setting special connection devices at the corners of the container, the corners will not slide under the action of small earthquakes, and the structure will maintain its overall working state; under the action of larger earthquakes, there is a certain displacement between the corner pieces. In this process, the "friction" between the corner pieces is used to consume seismic energy, reduce the propagation of seismic waves to the upper part of the structure, and make the structure basically in an elastic working state, thereby improving its seismic performance. IS is different from traditional steel structures in terms of seismic resistance. It mainly utilizes the discontinuity between the floors of container buildings to prevent or reduce the propagation of seismic waves to the upper structure of the structure, thereby reducing the seismic response of each floor.

2. Experimental Study

2.1. The Experimental Preparation

Considering that container steel (manufactured by CIMC (China International Marine Containers (Group) Co., Ltd.) in Shenzhen, China) is a special type of weather-resistant steel, material tests were conducted on its key components, as shown in Table 1. The experimental process was strictly carried out in accordance with the specifications [34–36].

Table 1. Material experiment for key components of containers.



Legend	Components	t	E	P	σ_y	σ_b
	Corner fitting	6	1.97	0.3	318.67	448.2
	Bottom side beam	4.5	2.01	0.3	318.44	458.07
	Top side beam	3	1.99	0.31	314.33	449.12
	Front corner post	6	1.97	0.3	318.67	448.2
	Rear corner post	6	1.97	0.3	318.67	448.2
	Side-wall	1.6	2.03	0.3	320.83	461.87
	Roof	2	2.04	0.28	325.89	476.21
	Front-wall	1.6	2.03	0.3	320.83	461.87

Note: l—The dimension in the length direction of the container (6058 mm). h—The dimension in the height direction of the component (2591 mm). w—The dimension in the width direction of the component (2438 mm). t—The thickness of specimen material (mm). E—The modulus of elasticity (10^5 MPa). P—The Poisson's ratio. σ_y—The yield strength (MPa). σ_b—The ultimate strength (MPa).

The experimental setup mainly includes a dedicated reaction frame for container testing, a standard 20 ft container, and a standard 40 ft container. In addition, to study the mechanical properties of the connected container, a dedicated container corner-fitting lock was also used, as shown in Figure 4. (The above experimental setup are all manufactured by CIMC in Shenzhen, China)

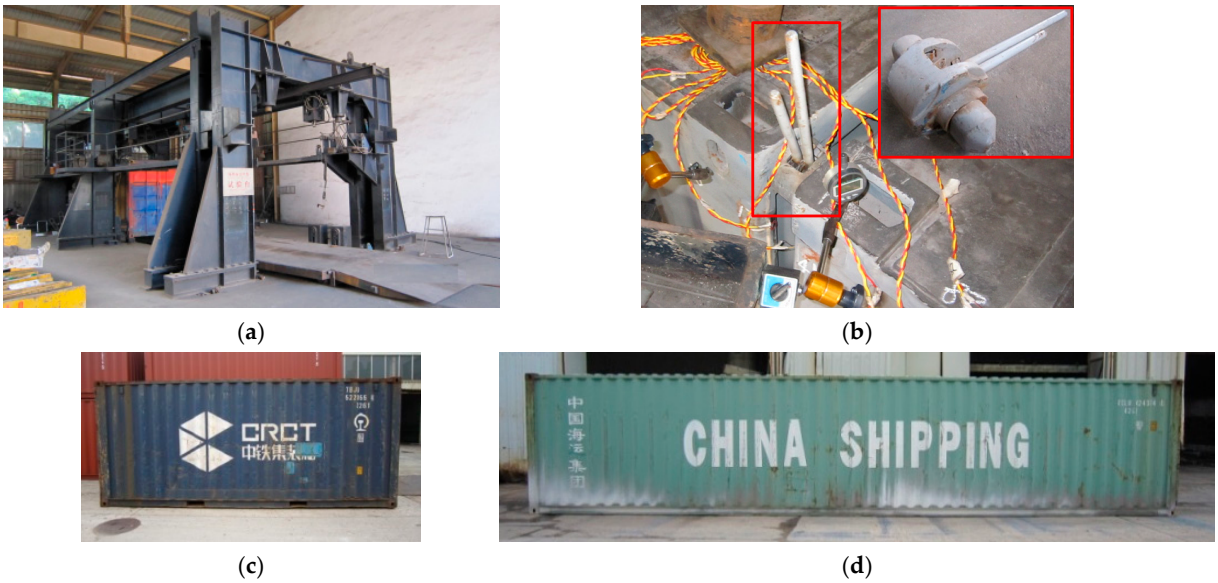
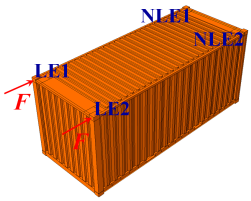
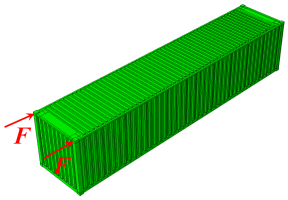
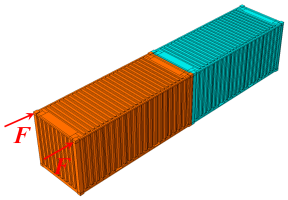


Figure 4. Experimental setup. (**a**) Reaction frame; (**b**) Container corner fitting lock; (**c**) Standard 20 ft container; (**d**) Standard 40 ft container.

The experimental setup is shown in Figure 5, where three forms of container stiffness were studied, namely 20C (20 ft container), 40C (40 ft container), and 20CC (connected 20 ft container). The load is a symmetrical longitudinal concentrated load applied to the two corner pieces at the top of the container. Based on finite element analysis, the loading program using load control is shown in Table 2. Due to the focus on studying the mechanical properties of the elastic stage, the load is continuously applied until a component of the container begins to yield. The constraints are fully applied to the four bottom corner pieces of the container and are in a completely fixed form [37,38].

Table 2. Loading program.

Container Category	Name	F_{max}	F_{max}/L	l
	20C	140	7	20
	40C	110	5.5	20
	20CC	140	7	20

Note: F—The load on a single-sided container (kN). F_{max}—The maximum load on a single-sided container (kN). l—The number of load levels.

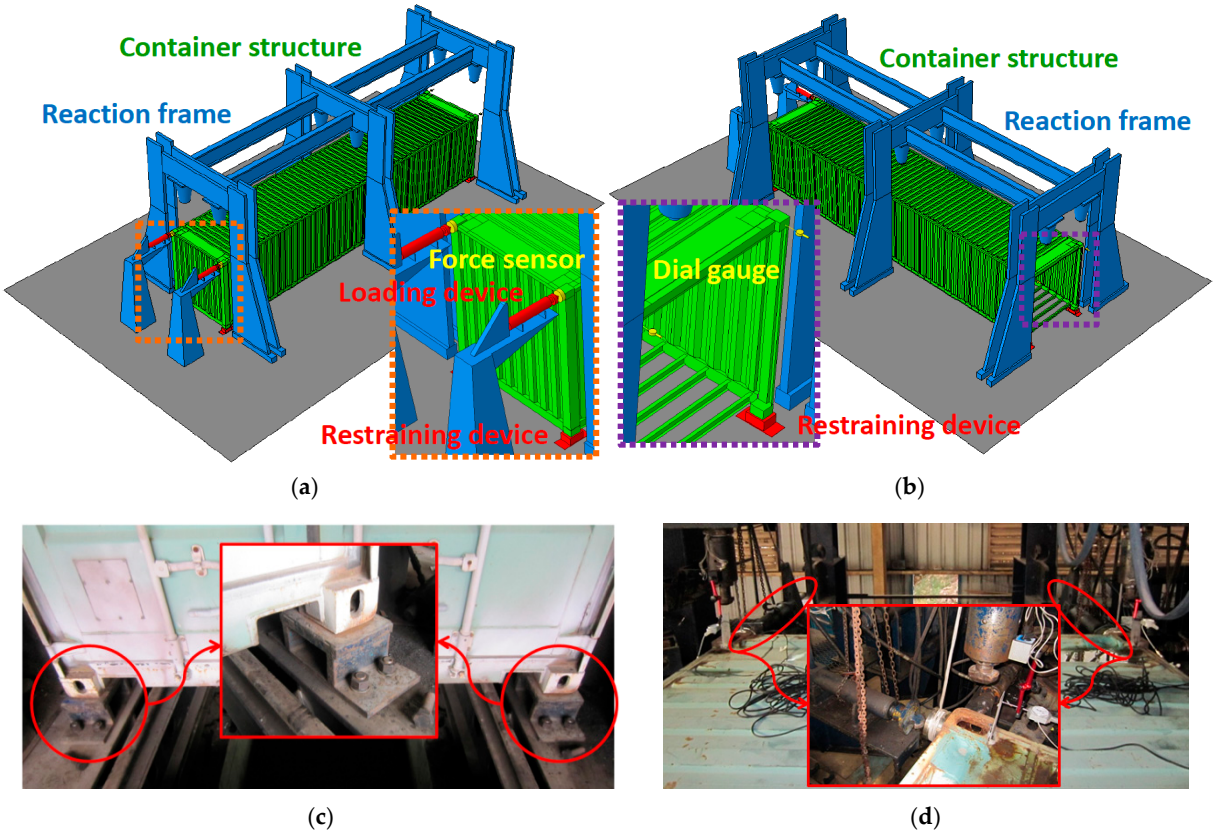


Figure 5. Experimental setup arrangement. (**a**) Overall schematic graph of LE; (**b**) Overall schematic graph of NLE; (**c**) Actual constraint graph; (**d**) Actual load graph. Note: LE—The loading end of the stiffness test for the container. NLE—The non-loading end of the stiffness test for the container.

2.2. The Experimental Results

From the load-displacement curves of LE1 and LE2, as well as NLE1 and NLE2, it can be seen that each curve is an oblique straight line, indicating that each experimental item is in the elastic stage, and each curve is symmetrically synchronized. Due to the applied load being a symmetrical concentrated synchronous load, the forces on both sides of the surface container are uniform and symmetrical, and there is no obvious torsion overall. When analyzing the force on the container, one side can be directly used, as shown in Figure 6.

From Figure 6, it can be seen that the stiffness of the container loading and non-loading ends for each experimental project is shown in Table 3. Based on the requirements of the literature [39,40], this article adopts the stiffness value of the container loading end as the overall stiffness value of the container. Due to the relatively low axial stiffness of the upper beam, its ability to transmit loads is limited, resulting in a much higher stiffness value at the non-loading end when testing the stiffness at the loading end. Based on experiments and finite element analysis, as the bottom side beams are not fixed, the side walls can deform freely, and the container as a whole exhibits a Z-shaped collapse deformation, which becomes more pronounced as the length of the container increases. Therefore, the stiffness of a 20 ft container should be greater than that of a 40 ft container; that is, the stiffness of experimental project 20C (58.07 kN/mm) is greater than that of 40C (33.41 kN/mm). It can be seen that as the length of the container increases, the stiffness of the container will gradually decrease. In terms of the connected container, namely 20CC, due to the small axial stiffness of the upper beam, its load transmission capacity is limited. Therefore, the overall deformation of the connected container is mainly concentrated on the first container, and the deformation at its non-loading end is very small, resulting in a small force on the second container. Therefore, the contribution of the second container to the overall stiffness

of the connected container is not significant; that is, the stiffness of 20CC (60.03 kN/mm) is slightly greater than that of 20C (58.07 kN/mm).

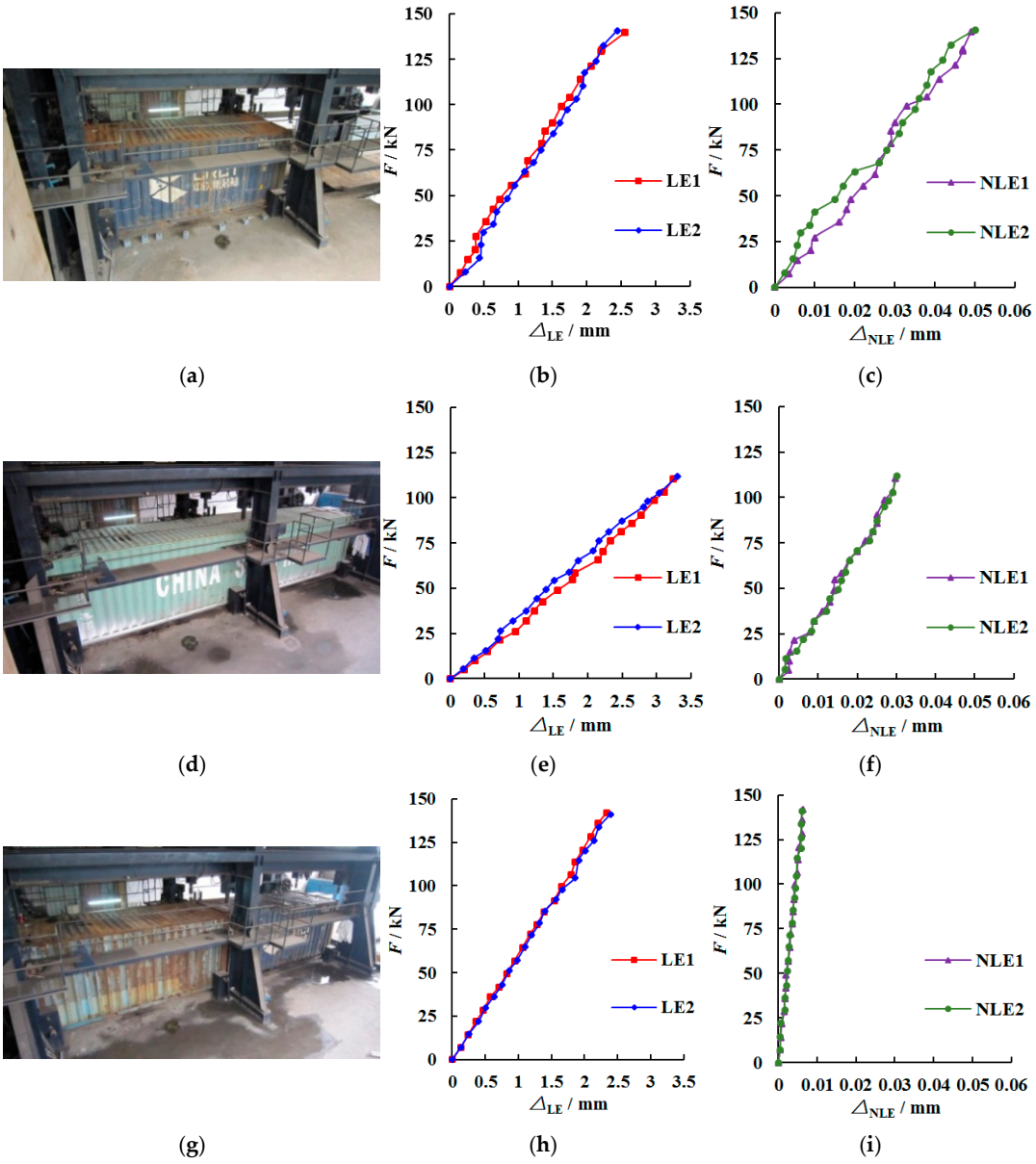


Figure 6. Load-displacement curves of the experiments. (**a**) Experimental project of 20C; (**b**) LE load displacement curve of 20C (LE); (**c**) NLE load displacement curve of 20C; (**d**) Experimental project of 40C; (**e**) LE load displacement curve of 40C; (**f**) NLE load displacement curve of 40C; (**g**) Experimental project of 20CC; (**h**) LE load displacement curve of 20CC; (**i**) NLE load displacement curve of 20CC. Note: Δ_{LE}—The loading end displacement (mm). Δ_{NLE}—The non-loading end displacement (mm).

Table 3. Container stiffness of each experimental item.

Container Category	20C		40C		20CC	
	F/Δ_{LE}	F/Δ_{NLE}	F/Δ_{LE}	F/Δ_{NLE}	F/Δ_{LE}	F/Δ_{NLE}
LE1 or NLE1	58.79	2755.22	32.44	3569.32	60.84	22,554.32
LE2 or NLE2	57.34	2904.80	34.38	3497.15	59.22	22,419.10
$k = 1/2(F/\Delta_{LE1} + F/\Delta_{LE2})$	58.07		33.41		60.03	
$2k$	116.14		66.82		120.06	

Note: k—The single side container stiffness (kN/mm). $2k$—The container stiffness (kN/mm).

3. Theoretical Analysis

Based on the common modular building structure of containers and the requirements of relevant specifications [39,41–43], this article establishes a six-story container house, which uses 20 ft containers of uniform specifications. Therefore, the mass of each floor is equal, and the friction coefficient between floors is equal. Sliding isolation devices are installed between adjacent upper and lower floors, and under certain conditions, friction sliding can occur between containers. The magnitude of the frictional force is taken as the Coulomb friction force, which is opposite to the direction of velocity and equal to the positive pressure multiplied by the friction coefficient. The structural model is shown in Figure 7.

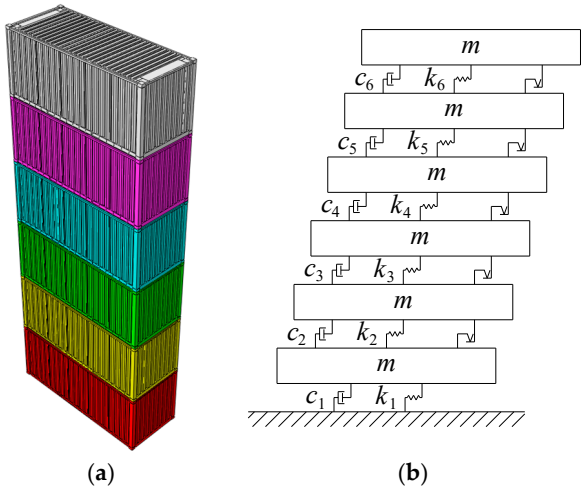


Figure 7. Six-story container module building structural model. (**a**) Actual model; (**b**) Mechanical calculation model of IS. Note: *c*—The container damping (N·s/m). *m*—The container mass (kg). *i*, *j*—The number.

3.1. Description of the IS

The proposed IS is designed specifically for multi-story modular container buildings to mitigate seismic response through friction energy dissipation at inter-layer interfaces. Unlike conventional isolation systems that require dedicated isolators (e.g., lead rubber bearings or friction pendulum bearings), the IS integrates the isolation function directly into the existing corner fitting connections, making it cost-effective and easy to implement.

The IS operates differently depending on the intensity of seismic excitation:

(1) Under frequent earthquakes (low seismic intensity). The inertial forces generated by the earthquake are insufficient to overcome the static friction at the interface. The corner fittings remain locked, and the container building behaves as a conventional non-isolated structure. No sliding occurs, and the building maintains its original configuration.

(2) Under rare earthquakes (high seismic intensity). When the inter-story shear force exceeds the maximum static friction force, relative sliding is initiated between the upper and lower corner fittings. During sliding, kinetic friction dissipates seismic energy as heat. The sliding displacement is limited by the length of the slotted hole. After the earthquake subsides, the structure may retain some residual displacement, but the superstructure remains essentially elastic, having been protected from direct transmission of strong ground motion.

3.2. Motion Equation of the Six-Story Isolation System

When establishing the structural motion equation, the following assumptions were made:

(1) The frictional force adopts Coulomb friction, which remains a constant throughout the process of structural motion;
(2) During the process of structural sliding, the overturning of the structure is not considered;
(3) Consider only horizontal seismic effects;
(4) Assuming sufficient sliding space at each corner;
(5) Assuming a low coefficient of friction, the structure is in a sliding state under seismic loads.

To ensure the validity of assumption (5)—i.e., the structure remains in a continuous sliding state under seismic loading—a criterion for the friction coefficient μ is required. Continuous sliding occurs when the imposed inertial force overcomes the maximum static friction force at each sliding interface. For the i-th layer with mass m_{i}, this condition is expressed as Equation (1).

$$\mu m_{\mathrm{i}} g \leq m_{\mathrm{i}} \mid \ddot{x}_{\mathrm{i}}(t) + \ddot{x}_{\mathrm{g}}(t) \mid_{\max} \tag{1}$$

where:

g—The gravity acceleration (m/s^2).

x—The displacement of each layer container to the ground (mm).

According to Figure 7, the dynamic motion equation of the structure is shown as Equation (2).

$$\boldsymbol{M}\ddot{\boldsymbol{x}} + \boldsymbol{C}\dot{\boldsymbol{x}} + \boldsymbol{K}\boldsymbol{x} + \boldsymbol{F}_{\mathbf{f}} = -\boldsymbol{M}\boldsymbol{I}\ddot{\boldsymbol{x}}_{\mathbf{g}} \tag{2}$$

where:

$\boldsymbol{M}$—The structure mass matrix.

$\boldsymbol{C}$—The structure damping matrix.

$\boldsymbol{K}$—The structure stiffness matrix.

$\boldsymbol{F}_{\mathbf{f}}$—The friction matrix between containers of each layer.

$\boldsymbol{I}$—The identity matrix.

$$\boldsymbol{M} = \begin{bmatrix} m & 0 & 0 & 0 & 0 & 0 \\ & m & 0 & 0 & 0 & 0 \\ & & m & 0 & 0 & 0 \\ & & & m & 0 & 0 \\ & & & & m & 0 \\ & & & & & m \end{bmatrix} \tag{3}$$

$$\boldsymbol{C} = \begin{bmatrix} c_1 + c_2 & -c_2 & 0 & 0 & 0 & 0 \\ & c_2 + c_3 & -c_3 & 0 & 0 & 0 \\ & & c_3 + c_4 & -c_4 & 0 & 0 \\ & & & c_4 + c_5 & -c_5 & 0 \\ & & & & c_5 + c_6 & -c_6 \\ & & & & & c_6 \end{bmatrix} \tag{4}$$

$$\boldsymbol{K} = \begin{bmatrix} k_1 + k_2 & -k_2 & 0 & 0 & 0 & 0 \\ & k_2 + k_3 & -k_3 & 0 & 0 & 0 \\ & & k_3 + k_4 & -k_4 & 0 & 0 \\ & & & k_4 + k_5 & -k_5 & 0 \\ & & & & k_5 + k_6 & -k_6 \\ & & & & & k_6 \end{bmatrix} \tag{5}$$

$$\boldsymbol{F_f} = \begin{Bmatrix} -5\mu mg\mathrm{sgn}(\dot{x}_2 - \dot{x}_1) \\ 5\mu mg\mathrm{sgn}(\dot{x}_2 - \dot{x}_1) - 4\mu mg\mathrm{sgn}(\dot{x}_3 - \dot{x}_2) \\ 4\mu mg\mathrm{sgn}(\dot{x}_3 - \dot{x}_2) - 3\mu mg\mathrm{sgn}(\dot{x}_4 - \dot{x}_3) \\ 3\mu mg\mathrm{sgn}(\dot{x}_4 - \dot{x}_3) - 2\mu mg\mathrm{sgn}(\dot{x}_5 - \dot{x}_4) \\ 2\mu mg\mathrm{sgn}(\dot{x}_5 - \dot{x}_4) - \mu mg\mathrm{sgn}(\dot{x}_6 - \dot{x}_5) \\ \mu mg\mathrm{sgn}(\dot{x}_6 - \dot{x}_5) \end{Bmatrix} \quad (6)$$

sgn(x)—The symbolic function. When x > 0, sgn(x) = 1; when x = 0, sgn(x) = 0; when x < 0, sgn(x) = −1.

For convenience, we set $x_2 - x_1 = u_2$, $x_3 - x_2 = u_3$, $x_4 - x_3 = u_4$, $x_5 - x_4 = u_5$, and $x_6 - x_5 = u_6$. And then Equation (2) can be transformed into Equation (7).

$$\begin{cases} m\ddot{x}_1 + c_1\dot{x}_1 + k_1x_1 - k_2u_2 - c_2\dot{u}_2 - 5\mu mg\mathrm{sgn}\dot{u}_2 = -m\ddot{x}_g \\ m\ddot{x}_2 + c_2\dot{u}_2 + k_2u_2 - k_3u_3 - c_3\dot{u}_3 + 5\mu mg\mathrm{sgn}\dot{u}_2 - 4\mu mg\mathrm{sgn}\dot{u}_3 = -m\ddot{x}_g \\ m\ddot{x}_3 + c_3\dot{u}_3 + k_3u_3 - k_4u_4 - c_4\dot{u}_4 + 4\mu mg\mathrm{sgn}\dot{u}_3 - 3\mu mg\mathrm{sgn}\dot{u}_4 = -m\ddot{x}_g \\ m\ddot{x}_4 + c_4\dot{u}_4 + k_4u_4 - k_5u_5 - c_5\dot{u}_5 + 3\mu mg\mathrm{sgn}\dot{u}_4 - 2\mu mg\mathrm{sgn}\dot{u}_5 = -m\ddot{x}_g \\ m\ddot{x}_5 + c_5\dot{u}_5 + k_5u_5 - k_6u_6 - c_6\dot{u}_6 + 2\mu mg\mathrm{sgn}\dot{u}_5 - \mu mg\mathrm{sgn}\dot{u}_6 = -m\ddot{x}_g \\ m\ddot{x}_6 + c_6\dot{u}_6 + k_6u_6 + \mu_6 mg\mathrm{sgn}\dot{u}_6 = -m\ddot{x}_g \end{cases} \quad (7)$$

3.3. Linear Equivalent of Motion Equation

The linear equivalent method is used to convert Equation (7) into linear equivalent equations, as shown in Equation (8).

$$\begin{cases} m\ddot{x}_1 + c_1\dot{x}_1 + k_1x_1 - k_2u_2 - c_{e2}\dot{u}_2 + e_1 = -m\ddot{x}_g \\ m\ddot{x}_2 + c_{e2}\dot{u}_2 + k_2u_2 - k_3u_3 - c_{e3}\dot{u}_3 + e_2 = -m\ddot{x}_g \\ m\ddot{x}_3 + c_{e3}\dot{u}_3 + k_3u_3 - k_4u_4 - c_{e4}\dot{u}_4 + e_3 = -m\ddot{x}_g \\ m\ddot{x}_4 + c_{e4}\dot{u}_4 + k_4u_4 - k_5u_5 - c_{e5}\dot{u}_5 + e_4 = -m\ddot{x}_g \\ m\ddot{x}_5 + c_{e5}\dot{u}_5 + k_5u_5 - k_6u_6 - c_{e6}\dot{u}_6 + e_5 = -m\ddot{x}_g \\ m\ddot{x}_6 + c_{e6}\dot{u}_6 + k_6u_6 + e_6 = -m\ddot{x}_g \end{cases} \quad (8)$$

where:

e_i—The error generated by the linear equivalent of i layer of structure, and can be expressed as Equation (9).

$$\begin{cases} e_1 = [(c_{e2} - c_2)\dot{u}_2 - 5\mu mg\mathrm{sgn}\dot{u}_2] \\ e_2 = [(c_{e3} - c_3)\dot{u}_3 - 4\mu mg\mathrm{sgn}\dot{u}_3] - [(c_{e2} - c_2)\dot{u}_2 - 5\mu mg\mathrm{sgn}\dot{u}_2] \\ e_3 = [(c_{e4} - c_4)\dot{u}_4 - 3\mu mg\mathrm{sgn}\dot{u}_4] - [(c_{e3} - c_3)\dot{u}_3 - 4\mu mg\mathrm{sgn}\dot{u}_3] \\ e_4 = [(c_{e5} - c_5)\dot{u}_5 - 2\mu mg\mathrm{sgn}\dot{u}_5] - [(c_{e4} - c_4)\dot{u}_4 - 3\mu mg\mathrm{sgn}\dot{u}_4] \\ e_5 = [(c_{e6} - c_6)\dot{u}_6 - \mu mg\mathrm{sgn}\dot{u}_6] - [(c_{e5} - c_5)\dot{u}_5 - 2\mu mg\mathrm{sgn}\dot{u}_5] \\ e_6 = -[(c_{e6} - c_6)\dot{u}_6 - \mu mg\mathrm{sgn}\dot{u}_6] \end{cases} \quad (9)$$

3.4. Error Minimization

The smaller the error term e_i, the smaller the error in the result of Equation (8). When the error term e_i can be neglected, Equation (8) is in the linear equation group, so it is necessary to minimize the e_i as follows.

3.4.1. Take Partial Derivative on the Square of the Expectations of the Error Term e_i

Take the partial derivative of the square of the expectations of the error term e_i, as shown in Equation (10).

$$\frac{\partial E({e_1}^2)}{\partial(c_{e2} - c_2)} = 2E[(c_{e2} - c_2){\dot{u}_2}^2 - 5\mu mg\dot{u}_2\mathrm{sgn}\dot{u}_2] = 0 \quad (10)$$

According to the literature [44,45], Equation (11) can be obtained.

$$c_{e2} = c_2 + 5\mu mg\frac{E(\dot{u}_2 \mathrm{sgn}\dot{u}_2)}{E{\dot{u}_2}^2} = c_2 + 5\mu mg\sqrt{\frac{2}{\pi}}\frac{1}{\sigma_{\dot{u}_2}} \tag{11}$$

where:

$\sigma_{\dot{u}_i}$—The mean square deviation of $\dot{u}_i$.

According to Equation (10), Equation (12) can be obtained.

$$\frac{\partial^2 E({e_1}^2)}{\partial(c_{e2} - c_2)^2} = 2E({\dot{u}_2}^2) > 0 \tag{12}$$

When Equation (10) is established, e_1 it takes its minimum value. Then, assuming that $e_1 = 0$, from Equations (9) and (11), Equation (13) can be obtained.

$$\frac{\mathrm{sgn}\dot{u}_2}{\dot{u}_2} = \sqrt{\frac{2}{\pi}}\frac{1}{\sigma_{\dot{u}_2}} \tag{13}$$

3.4.2. Take Partial Derivative on the Square of the Error Term e_2

Take the partial derivative of the square of the error term e_2, as shown in Equation (14).

$$\frac{\partial({e_2}^2)}{\partial(c_{e3} - c_3)} = 2\dot{u}_3\{[(c_{e3} - c_3)\dot{u}_3 - 4\mu mg\mathrm{sgn}\dot{u}_3] - [(c_{e2} - c_2)\dot{u}_2 - 5\mu mg\mathrm{sgn}\dot{u}_2]\} = 0 \tag{14}$$

As $\dot{u}_3$ is a change value, Equation (15) can be obtained.

$$e_2 = [(c_{e3} - c_3)\dot{u}_3 - 4\mu mg\mathrm{sgn}\dot{u}_3] - [(c_{e2} - c_2)\dot{u}_2 - 5\mu mg\mathrm{sgn}\dot{u}_2] = 0 \tag{15}$$

As $e_1 = 0$, Equation (16) can be obtained.

$$e_2 = (c_{e3} - c_3)\dot{u}_3 - 4\mu mg \cdot \mathrm{sgn}\dot{u}_3 = 0 \tag{16}$$

Equation (17) can be obtained.

$$c_{e3} = c_3 + 4\mu mg\frac{\mathrm{sgn}\dot{u}_3}{\dot{u}_3} = c_3 + 4\mu mg\sqrt{\frac{2}{\pi}}\frac{1}{\sigma_{\dot{u}_3}} \tag{17}$$

In the same way, Equations (18)–(20) can be obtained.

$$c_{e4} = c_4 + 3\mu mg\frac{\mathrm{sgn}\dot{u}_4}{\dot{u}_4} = c_4 + 3\mu mg\sqrt{\frac{2}{\pi}}\frac{1}{\sigma_{\dot{u}_4}} \tag{18}$$

$$c_{e5} = c_5 + 2\mu mg\frac{\mathrm{sgn}\dot{u}_4}{\dot{u}_4} = c_5 + 2\mu mg\sqrt{\frac{2}{\pi}}\frac{1}{\sigma_{\dot{u}_5}} \tag{19}$$

$$c_{e6} = c_6 + \mu mg\frac{\mathrm{sgn}\dot{u}_4}{\dot{u}_4} = c_6 + \mu mg\sqrt{\frac{2}{\pi}}\frac{1}{\sigma_{\dot{u}_6}} \tag{20}$$

And then, the equivalent damping ratio of i layer of structure can be expressed as Equation (21).

$$\varsigma_{ei} = \varsigma + \frac{\mu g}{\omega_i}\frac{1}{\sqrt{2\pi\sigma^2_{\dot{u}_i}}} \tag{21}$$

where:

ς_{ei}—The equivalent damping ratio of i layer of structure.

ζ—The damping ratio.
ω—The self-vibration frequency (rad/s).

3.5. Mean Squared Error Formula of Speed

3.5.1. Motion Equation Simplify

When solving $\sigma_{\dot{u}_i}$, it can be assumed that only the i layer will slide, and structures below the i layer are considered as rigid structures and move together with the ground; the structures above i layer are assumed to move to the displacement limit without relative sliding, so the calculation diagram of the multi-layer seismic isolation container structure is shown in Figure 8. So, at this point, the structure is equivalent to a structure with a bottom friction sliding isolation device.

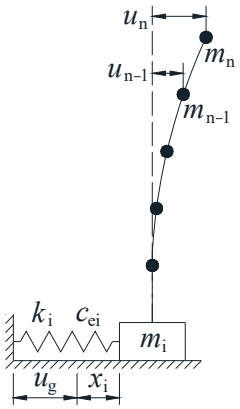


Figure 8. Multi-layer isolated container structure equivalent system.

For Figure 8, the motion equation of the structure is divided into two parts: the first part is the relative vibration of the particle of the upper part, and the second part is the joint vibration of the particle i and its upper structure. The motion equation is given in Equations (22) and (23).

$$M_s\ddot{u} + C_s\dot{u} + K_s u = -(\ddot{u}_g + \ddot{x}_i)M_s I \tag{22}$$

$$m_i(\ddot{u}_g + \ddot{x}_i) + I^T M_s(\ddot{u}_g + \ddot{x}_i + \ddot{u}) + c_{ei}\dot{x}_i + k_i x_i = 0 \tag{23}$$

According to Equation (23), Equation (24) can be obtained.

$$I^T M_s\ddot{u} + m_z\ddot{x}_i + c_{ei}\dot{x}_i + k_i x_i = -m_z\ddot{u}_g \tag{24}$$

In Equation (24), the first item is the inertia force of all particle masses above i layer of structure, as shown in Equation (25).

$$I^T M_s\ddot{u} = m_{i+1}\ddot{u}_{i+1} + m_{i+2}\ddot{u}_{i+2} + \cdots + m_n\ddot{u}_n \tag{25}$$

As Figure 8 shows, since there is $u_i \ll x_i$ and $m_i \ll m_z$, the item in Equation (25) can be deleted, and, according to Equation (24), the approximate motion equation can be obtained, as shown.

$$m_z\ddot{x}_i + c_{ei}\dot{x}_i + k_i x_i = -m_z\ddot{u}_g \tag{26}$$

According to Equations (22) and (26), the system is decomposed into two parts.

3.5.2. The Mean Variance of Speed

According to the structure, as shown in Figure 8 and Equation (26), Equation (27) can be obtained.

$$\ddot{x}_i + 2\varsigma_{ei}\omega_i\dot{x}_i + \omega_i^2 x_i = -\ddot{u}_g \tag{27}$$

According to the literature [44,45], when the spectral density constant of white noise S_0 = 55.44 cm^2/s^3, the acceleration of the ground due to an earthquake can be simulated by white noise. So the acceleration of the ground $\ddot{u}_g$ can be expressed as Equation (28).

$$\begin{cases} \ddot{u}_g = e(t)W(t) \\ \langle W(t)\rangle = 0 \\ \langle W(t)W(t+\tau)\rangle = 2\pi S_0\delta(\tau) \end{cases} \tag{28}$$

where:

S_0—The spectral density constant of white noise (m^2/s^3).

e(t)—The envelope function.

W(t)—The steady process of white noise (m/s^2).

< >—The overall mean.

$\delta(\tau)$—The Dirac function.

According to the literature [44,45], using the relationship between the correlation function and spectral density together with the Fourier transform formula, the correlation function of stationary white noise can be obtained, as shown in Equations (29) and (30).

$$R_g(\tau) = 2\pi S_0\delta(\tau) \tag{29}$$

$$\begin{aligned} R_{xx}(t_1,t_2) &= \frac{2\pi S_0}{\omega_d^2}\int_0^{t_1}\int_0^{t_2}\delta(s_1-s_2)e^{-\varsigma_{ei}\omega_i(t_1-s_1)}\sin[\omega_d(t_1-s_1)]e^{-\varsigma_{ei}\omega_i(t_2-s_2)}\sin[\omega_d(t_2-s_2)]ds_1ds_2 \\ &= \frac{2\pi S_0}{\omega_d^2}\int_0^{\min(t_1,t_2)} e^{-\varsigma_{ei}\omega_i(t_1+t_2-2s)}\sin[\omega_d(t_1-s)]\sin[\omega_d(t_2-s)]ds \\ &= \frac{\pi S_0}{2\varsigma_{ei}\omega_i^3}\left\{e^{-\varsigma_{ei}\omega_i|t_2-t_1|}[\cos(\omega_d(t_2-t_1)) + \frac{\varsigma_{ei}\omega_i}{\omega_d}\sin(\omega_d(t_2-t_1))] + e^{-\varsigma_{ei}\omega_i|t_2+t_1|}\times\cdots\right\} \end{aligned} \tag{30}$$

where: $\omega_d = \omega_0\sqrt{1-\varsigma^2}$, ω_0 is the natural circle frequency $\omega_0 = \sqrt{k/m}$.

When $t \to \infty$, Equation (30) can be expressed as Equation (31).

$$\begin{aligned} R_{xx}(t_1,t_2) = R_{xx}(\tau) &= \frac{\pi S_0}{2\varsigma_{ei}\omega_i^3}e^{-\varsigma_{ei}\omega_i|t_2-t_1|}[\cos(\omega_d(t_2-t_1)) + \frac{\varsigma_{ei}\omega_i}{\omega_d}\sin(\omega_d(t_2-t_1))] \\ &= \frac{\pi S_0}{2\varsigma_{ei}\omega_i^3}e^{-\varsigma_{ei}\omega_i\tau}[\cos(\omega_d\tau) + \frac{\varsigma_{ei}\omega_i}{\omega_d}\sin(\omega_d\tau)] \end{aligned} \tag{31}$$

And then, Equation (32) can be obtained.

$$R_{\dot{x}\dot{x}}(\tau) = -\frac{d^2R_x(\tau)}{d\tau^2} = \frac{\pi S_0}{2\varsigma\omega_i}e^{-\varsigma_{ei}\omega_i\tau}[\cos(\omega_d\tau) - \frac{\varsigma_{ei}\omega_i}{\omega_d}\sin(\omega_d\tau)] \tag{32}$$

So the speed mean variance of the steady stage can be expressed as Equation (33).

$$\sigma_{\dot{x}}^2 = R_{\dot{x}\dot{x}}(0) = \frac{\pi S_0}{2\varsigma_{ei}\omega_i} \tag{33}$$

According to Equations (21), (33), and (34) can be obtained.

$$\sigma_{\dot{x}_i}^2 = \frac{\mu^2 g^2}{8\omega_i^2\varsigma^2\pi}\left(\sqrt{1+\frac{4\pi^2\omega_i S_0\varsigma}{\mu^2 g^2}}+1\right)^2 \tag{34}$$

Substitute Equation (34) into Equation (21). Thus, the equivalent damping ratio of each layer can be obtained as shown in Equation (35).

$$\varsigma_{ei} = \varsigma + \frac{2\varsigma}{\sqrt{1 + \frac{4\pi^2 \omega_i S_0 \varsigma}{\mu^2 g^2}} + 1} \tag{35}$$

3.6. An Example of a Sliding Isolation Structure of Six Layers

A building is a six-layer container structure with slip isolation of each layer. A 20 ft standard container is used, the structural damping ratio is taken as 0.05, the mass of each layer is taken as 2230 kg, the friction coefficient between layers is taken as 0.15, the container stiffness is taken as 58.07 kN/mm, 33.41 kN/mm, and 60.03 kN/mm, and the spectral density constant of white noise S_0 is taken as 55.44 cm^2/s^3.

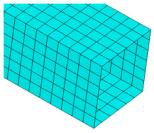
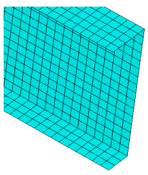
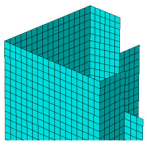
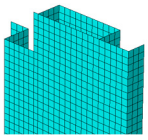
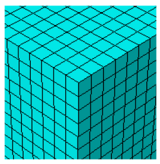
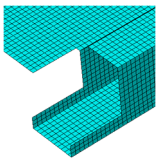
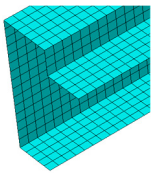
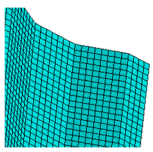
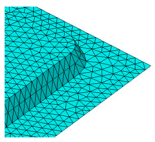
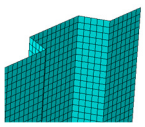
According to the above parameters and Equation (34), the equivalent damping ratios of the second to sixth layers can be obtained as 0.090, 0.089, 0.088, 0.087, and 0.084, respectively, for the 20 ft container, and 0.126, 0.123, 0.120, 0.115, and 0.110, respectively, for the 40 ft container.

4. Finite Element Simulation

4.1. Establishment of Finite Element Model

A six-story container building model was established using the large-scale nonlinear finite element software Abaqus 6.14 (manufactured by Dassault Systemes in Paris, France) [46,47]. The technical parameters of the container model element are shown in Table 4.

Table 4. The element of the container model.

Member Name	**Top Side Beam**	**Bottom Side Beam**	**Front Corner Column**	**Rear Corner Column**	**Corner Fitting**
Member form					
Size/mm	15	15	15	15	10
Shape	Quad	Quad	Quad	Quad	Hex
Technique	Structured	Structured	Structured	Structured	Structured
Type	S4R	S4R	S4R	S4R	C3D8R
Member Name	**Top end beam**	**Bottom end beam**	**Side wall**	**Top wall**	**End wall**
Member Form					
Size/mm	15	15	10	10	10
Shape	Quad	Quad	Quad	Tri	Quad
Technique	Structured	Structured	Structured	Free	Structured
Type	S4R	S4R	S4R	S3	S4R

The material parameters and constitutive relationships in the finite element model can be found in Table 1 and Figure 9.

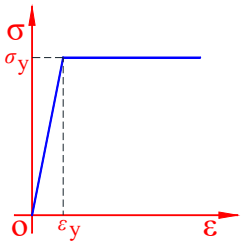


Figure 9. Material constitutive model of the container. Note: *O*—The origin coordinates. σ—The stress coordinate axis. ε—The strain coordinate axis. ε_y—The yield strain.

The dimensions of the main container component are shown in Figure 10. More detailed dimensions can be found in the literature [1,35].

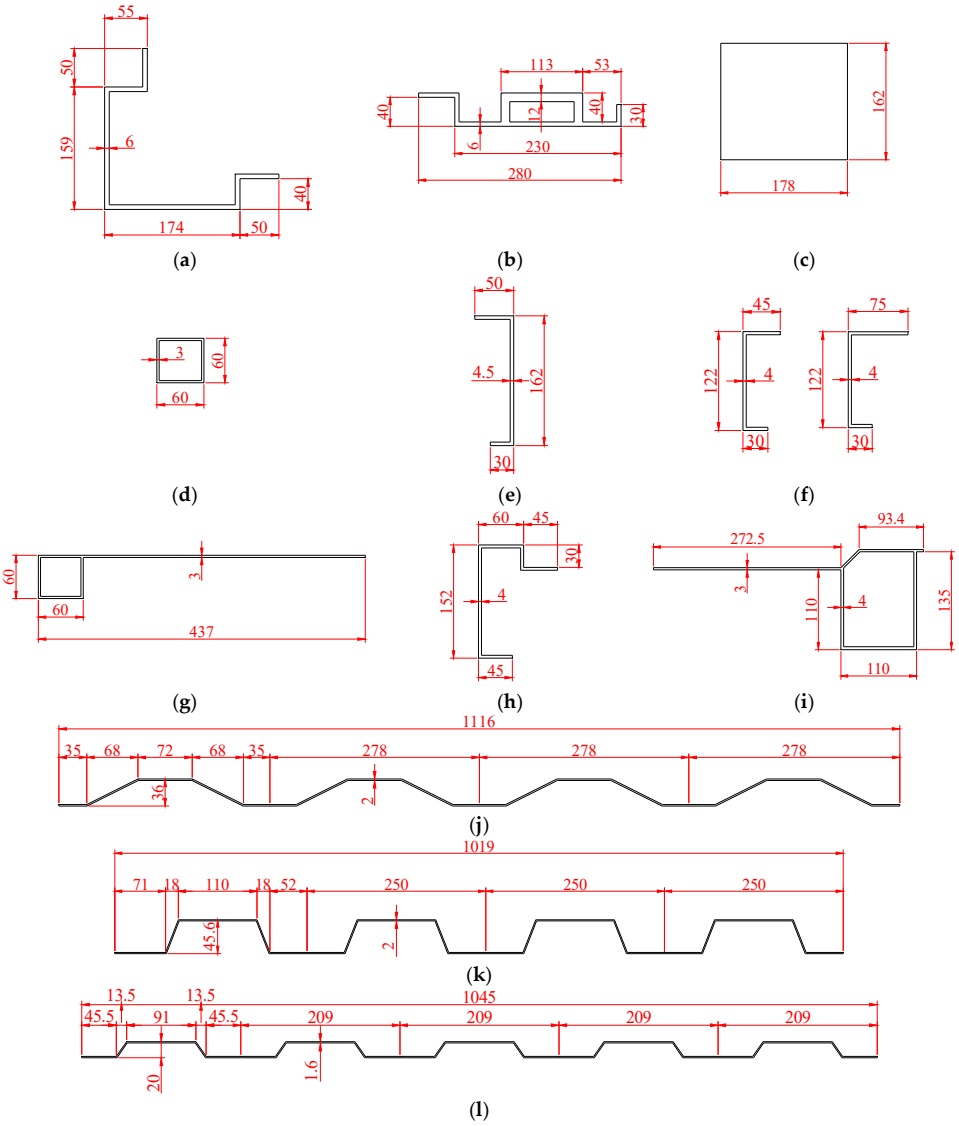
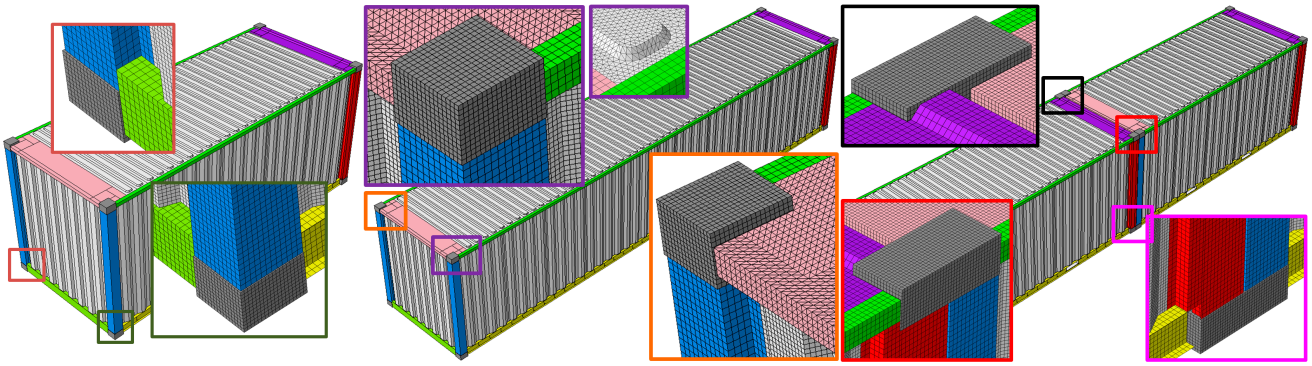


Figure 10. The dimensions of the main container component (mm). (**a**) The front corner column (*h*c = 2325); (**b**) The rear corner column (*h*c = 2325); (**c**) The corner fitting (*h*c = 118); (**d**) The bottom side beam (*l*c = 5720); (**e**) The top side beam (*l*c = 5720); (**f**) The bottom beam (*w*c = 2332); (**g**) The top end beam (*w*c = 2114); (**h**) The bottom end beam (*w*c = 2114); (**i**) The door header (*w*c = 2114); (**j**) The corrugated sheet of side wall (*h*c = 2325); (**k**) The corrugated sheet of end wall (*h*c = 2325); (**l**) The corrugated sheet of roof (*w*c = 2356). Note: *h*c—The dimension in the height direction of the component (mm). *l*c—The dimension in the length direction of the component (mm). *w*c—The dimension in the width direction of the component (mm).

Based on the above analysis, the nonlinear finite element model of the container building structure is shown in Figure 11.



(**a**) (**b**) (**c**)

Figure 11. Container building structure model. (**a**) 20C; (**b**) 40C; (**c**) 20CC.

Based on finite element analysis, the container stiffness values of each test item were obtained and compared with the test results, as shown in Table 5.

Table 5. Experiment and finite element method comparison of container stiffness.

Container Category	**20C**					
	F/Δ_{LE}			F/Δ_{NLE}		
	E	**FEM**	E_{EFEM}	**E**	**FEM**	E_{EFEM}
LE1 or NLE1	58.79	61.18	3.57%	2755.22	2916.5	4.78%
LE2 or NLE2	57.34	61.18	5.59%	2904.80	2916.5	4.48%
$k = 1/2\ (F/\Delta_{LE1} + F/\Delta_{LE2})$	58.07	61.18	4.56%	—	—	—
$2k$	116.14	122.36	4.57%		—	—
Container category	**40C**					
	F/Δ_{LE}			F/Δ_{NLE}		
	E	**FEM**	E_{EFEM}	**E**	**FEM**	E_{EFEM}
LE1 or NLE1	32.44	34.78	5.20%	3569.32	3718	3.97%
LE2 or NLE2	34.38	34.78	4.29%	3497.15	3718	5.27%
$k = 1/2\ (F/\Delta_{LE1} + F/\Delta_{LE2})$	33.41	34.78	4.73%	—	—	—
$2k$	66.82	69.56	4.74%	—	—	—
Container category	**20CC**					
	F/Δ_{LE}			F/Δ_{NLE}		
	E	**FEM**	E_{EFEM}	**E**	**FEM**	E_{EFEM}
LE1 or NLE1	60.84	64.55	6.10%	22,554.32	24,120.32	6.94%
LE2 or NLE2	59.22	64.55	9.00%	22,419.10	24,120.32	7.59%
$k = 1/2\ (F/\Delta_{LE1} + F/\Delta_{LE2})$	60.03	64.55	7.53%	—	—	—
$2k$	120.06	129.10	7.53%	—	—	—

Note: E—The experiment method. FEM—The finite element method. E_{EFEM}—The error between experiment and finite element method (%).

Based on the above analysis, the nonlinear finite element model of the six-story container building structure is shown in Figure 12. Among them, the upper and lower containers are fixed by corner pieces, and the overall container building structure is fixed to the ground by corner pieces and bottom beams. The seismic fortification intensity of this structure is

9 degrees, the design basic seismic acceleration is 0.4 g, the site type is Class II, and the design earthquake group is Group I. For NIS-sdr and NIS-edr, tie connections are established between the upper and lower containers; For IS, a sliding contact connection is established between the upper and lower containers. Friction force is selected based on Coulomb friction, with a friction coefficient of 0.15 and a maximum slip between layers of 42 mm.

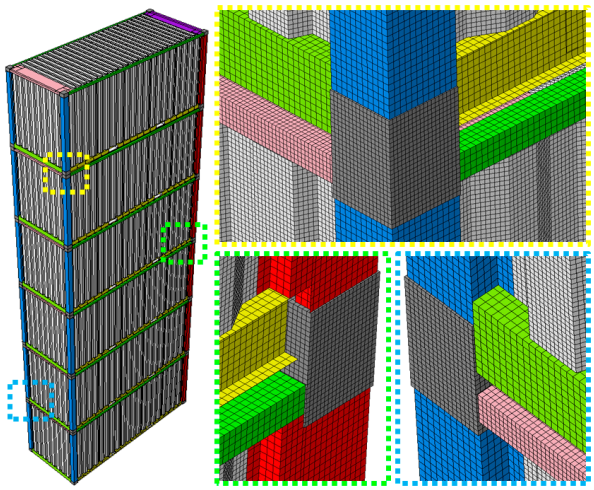


Figure 12. Six-story container building structure model.

4.2. IS Technical Requirements

To ensure reliable performance, the IS must satisfy the technical requirements specified in Table 6. These requirements cover friction coefficient, slotted hole geometry, surface treatment, material properties, and load capacity.

Table 6. Technical requirements for the IS.

Parameter	Requirement	Acceptable Range	Test Method
Friction coefficient μ	0.12–0.20 (static), 0.10–0.18 (kinetic)	±0.03	Inclined plane test
Slotted hole length	35–50 mm (depending on seismic intensity)	±2 mm	Direct measurement
Slotted hole width	22 mm (for M20 bolt)	±0.5 mm	Direct measurement
Contact surface roughness	0.8–1.6 μm	±0.2 μm	Profilometer
Friction material (optional)	Brass or PTFE composite	—	—
Vertical load capacity	≥150 kN per corner fitting	—	Compression test
Bolt preload (if used)	50–100 kN	±10 kN	Torque wrench
Sliding cycles durability	≥50 cycles without degradation	—	Cyclic sliding test

Two key parameters govern the performance of the IS:

(1) Friction coefficient. This determines the threshold for initiating sliding. A lower μ allows earlier sliding and more energy dissipation but may lead to excessive residual displacement. A higher μ delays sliding but reduces the risk of residual displacement.
(2) Slotted hole length. This determines the maximum allowable slip distance and should be designed to accommodate the expected inter-story displacement under rare earthquakes without causing collision or dislodgment.

4.3. Modal and Damping

Modal [48] is the inherent vibration characteristic of a structure. Table 7 shows the periods of the first eight order formations obtained by Abaqus modal analysis using NIS-sdr

and NIS-edr. The first period of the structure is 0.412 s, and the second period is 0.143 s. The first period is approximately three times the second period. Therefore, the dynamic response of the container structure is controlled by the first mode.

Table 7. Various modes of vibration.

Modal Order	1	2	3	4	5	6	7	8
T/s	0.412	0.143	0.134	0.133	0.131	0.121	0.098	0.093
ω/rad/s	15.278	43.967	46.764	47.200	47.660	52.088	64.359	67.456

Note: T—The period (s).

Damping [49] is an important factor affecting the dynamic response of structures. Rayleigh damping indicates that the damping matrix is a linear combination of the mass matrix and the stiffness matrix, as shown in Equation (36).

$$[C] = \alpha[M] + \beta[K] \tag{36}$$

where:

α, β—The constant.

$\alpha = 2\omega_i\omega_j\frac{\xi_j\omega_i - \xi_i\omega_j}{\omega_i^2 - \omega_j^2}$.

$\beta = 2\frac{\xi_j\omega_i - \xi_i\omega_j}{\omega_i^2 - \omega_j^2}$.

According to reference [45], in the elastic-plastic analysis under rare earthquakes, the damping ratio of steel structures can be taken as 0.05. Assuming that the damping ratios of each mode are the same and the frequencies of the first two modes are taken, the calculated values of α = 1.1339 and β = 0.001688 for NIS-sdr and NIS-edr can be obtained.

From the above analysis, according to Equation (35), the equivalent damping ratios of the second to sixth layers are 0.090, 0.089, 0.088, 0.087, and 0.084, respectively. Therefore, the IS equivalent damping ratio can be calculated according to Equation (37).

$$\xi_{eq} = \sum K_j\xi_{eqj} / \sum K_j \tag{37}$$

where:

ξ_{eq}—The equivalent damping ratio of the overall structure.

ξ_{eqj}—The equivalent damping ratio of the j isolation layer structure.

K_j—The horizontal stiffness of the j isolation layer structure.

According to the calculation, the equivalent damping ratio of IS is 0.081, resulting in α = 1.8369 and β = 0.002735 for IS.

4.4. Elastic-Plastic Time-History Analysis of Structure

4.4.1. The Selection of Seismic Wave

In the time-history analysis, the selected seismic waves mainly include typical strong earthquake records, fitted artificial waves, and actual seismic records of the proposed site. Among them, the best approach is to use the actual seismic records of the constructed site, but it is difficult to achieve this. Therefore, in practical time-history analysis, some existing typical seismic waves are often selected for structural seismic calculations, such as the EL-Centro wave, Taft wave, etc. In addition, when selecting seismic waves, the engineering geological conditions of the location of the structure should also be considered. According to the literature [45], when using the time-history analysis method, actual strong earthquake records and artificially simulated acceleration time-history curves should be selected according to the type of building site and the design earthquake group. The number

of actual strong earthquake records should not be less than 2/3 of the total number, and the average seismic influence coefficient curve of multiple time-history curves should be consistent with the seismic influence coefficient curve used in the mode decomposition response spectrum method in terms of statistical significance. The maximum value of the acceleration time-history can be used according to Table 8.

Table 8. The maximum value of seismic acceleration time-history used in time-history analysis.

Earthquake Impact	6-Degree	7-Degree	8-Degree	9-Degree
Frequent earthquakes/cm/s^2	18	35 (55)	70 (110)	140
Rare earthquake occurrence/cm/s^2	125	220 (310)	400 (510)	620

Note: The values in parentheses are used for areas with designed basic seismic accelerations of 0.15 g and 0.30 g, respectively.

The base acceleration and frequency spectrum of the El-Centro wave, the Taft wave, and the artificial wave are as follows.

(1) El-Centro wave: (1) Basic acceleration: The N-S component is 341.7 cm/s^2, the E-W component is 210.1 cm/s^2, and the U-D component is 206.3 cm/s^2. (2) Spectral characteristics: The main frequencies are concentrated in the range of 1–3 Hz, with rich mid to high frequency components, belonging to typical near-field strong earthquake records.

(2) Taft wave: (1) Basic acceleration: It is 178 cm/s^2 (the specific value may vary slightly depending on the component and processing method). (2) Spectral characteristics: The main frequency range is about 0.5–5 Hz, belonging to the category of far-field seismic waves, with a wide frequency band, multi-peak characteristics, and uniform energy distribution.

(3) Artificial wave: (1) Basic acceleration: The peak acceleration of the artificial wave is set according to design requirements and is usually adjusted based on the literature [45]. This article uses rare earthquakes in the 9-degree zone (620 cm/s^2). (2) Spectral characteristics: The spectrum is generated based on the design response spectrum, covering the main natural period range of the structure, and can reflect the seismic characteristics of specific site conditions, making the artificial wave approach real earthquakes in terms of spectrum shape, duration, and energy distribution.

Therefore, three seismic waves were selected for the structural analysis process, namely the EL-Centro wave, the Taft wave, and the artificial wave. In the time-history analysis, the duration of seismic waves is taken as 15 s, and the time interval is 0.02 s.

The acceleration time-histories of the three seismic waves were scaled to match the target peak ground acceleration (PGA) of 620 cm/s^2 for rare earthquakes under 9-degree intensity, as shown in Table 8. The scaling factors applied are: 1.81 for the EL-Centro wave (original PGA = 341.7 cm/s^2), 3.48 for the Taft wave (original PGA = 178 cm/s^2), and 1.00 for the artificial wave (generated to match 620 cm/s^2).

Table 9 summarizes the spectral compatibility check results. The following criteria from the literature [35] are evaluated:

(1) In the predominant period range of the structure (0.1 s to 1.0 s, covering the first three natural periods of 0.412 s, 0.143 s, and 0.134 s, as shown in Table 7), the average response spectrum shall not deviate below the target spectrum by more than 20%.

(2) For each individual seismic wave, the deviation from the target spectrum shall not exceed 35%.

Table 9. Spectral compatibility check of selected seismic waves with the target design response spectrum.

Seismic Wave	PGA Scaling Factor	Max. Positive Deviation/%	Max. Negative Deviation/%
EL-Centro wave	1.81	+18% (T = 0.15 s)	−15% (T = 0.45 s)
Taft wave	3.48	+28% (T = 0.20 s)	−22% (T = 0.60 s)
Artificial wave	1.00	+12% (T = 0.25 s)	−8% (T = 0.50 s)
Average of three waves	—	+8% (T = 0.25 s)	−12% (T = 0.40 s)
Allowable limit	—	≤35% (individual)/≤20% (average)	—

4.4.2. Displacement of Top Point of Structure

Figure 13 shows the top point of the time-history curve of NIS-sdr under three seismic waves. Figure 14 shows the top point in the time-history curve of NIS-edr under three seismic waves. Figure 15 shows the top point in the time-history curve of IS under three seismic waves. According to the time-history curve:

(1) In the same intensity region, at the same level, the structural displacement response is different from the input of the seismic waves. Among them, the structural displacement response is the largest under the Taft wave, while the structural displacement response is the minimum under the EL-Centro wave. This shows that the spectral characteristics of seismic waves will obviously affect the structural dynamic response.
(2) Compared with Figures 13–15, the displacement response of IS is greatly reduced. This shows that the IS can effectively reduce the seismic response.
(3) As seen from Figure 15, because the structure has a sliding isolation device, the vertex displacement curve of the IS is not always around the horizontal axis.

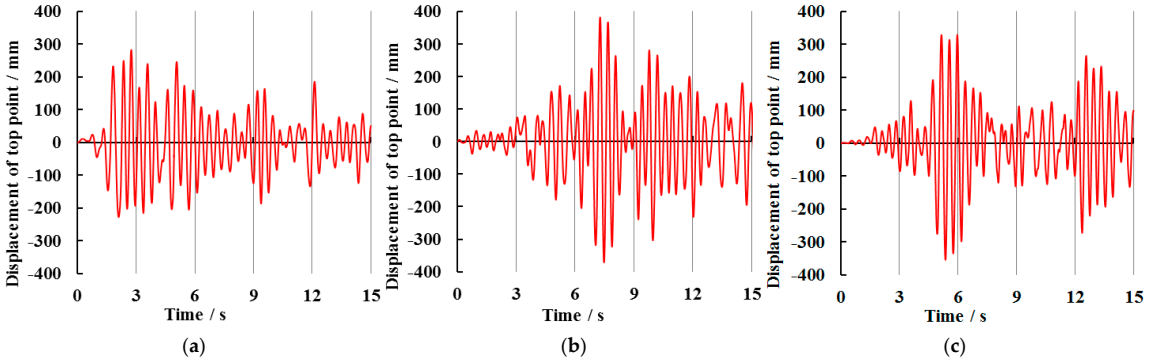


Figure 13. Top displacement-time curve of NIS-sdr. (**a**) Transverse EL-Centro wave; (**b**) Transverse Taft wave; (**c**) Transverse artificial wave.

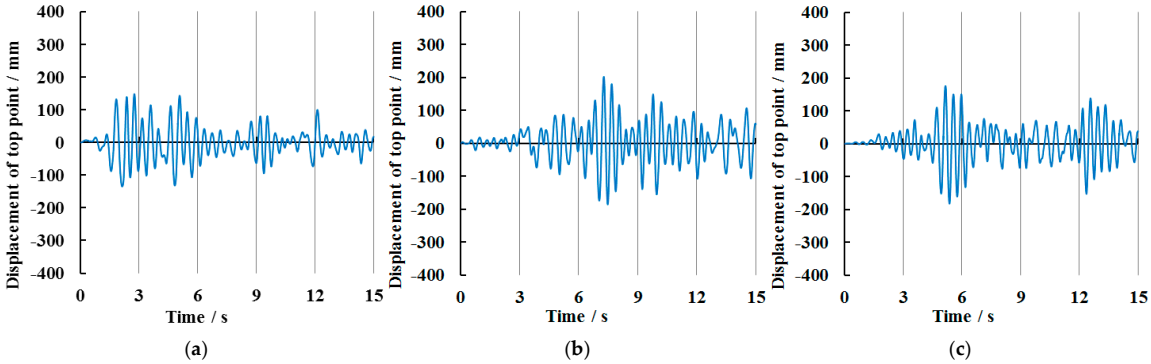


Figure 14. Top displacement-time curve of NIS-edr. (**a**) Transverse EL-Centro wave; (**b**) Transverse Taft wave; (**c**) Transverse artificial wave.

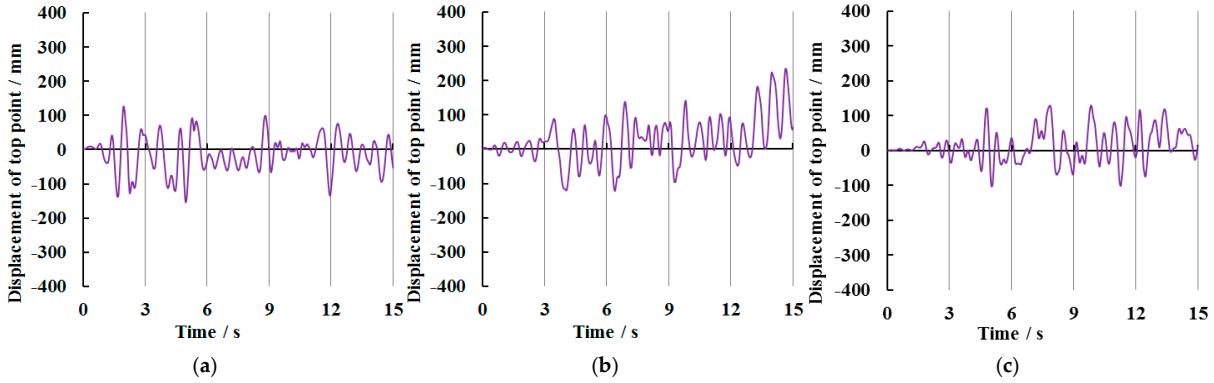


Figure 15. Top displacement-time curve of IS. (**a**) Transverse EL-Centro wave; (**b**) Transverse Taft wave; (**c**) Transverse artificial wave.

4.4.3. Maximum Displacement of Each Layer of Structure

According to the literature [45], three seismic waves are selected in this paper, and the maximum displacement of the structure under different seismic loading is shown in Figure 16. It can be seen that the stiffness of the structure is uniformly distributed along the vertical direction, without any weak layers. The IS can effectively reduce the maximum displacement of each floor of the structure.

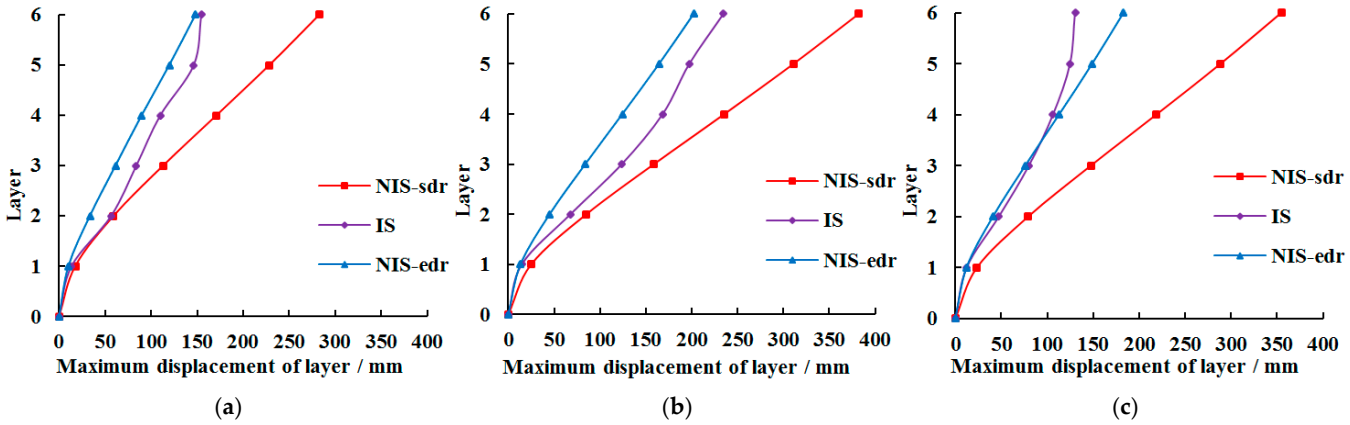
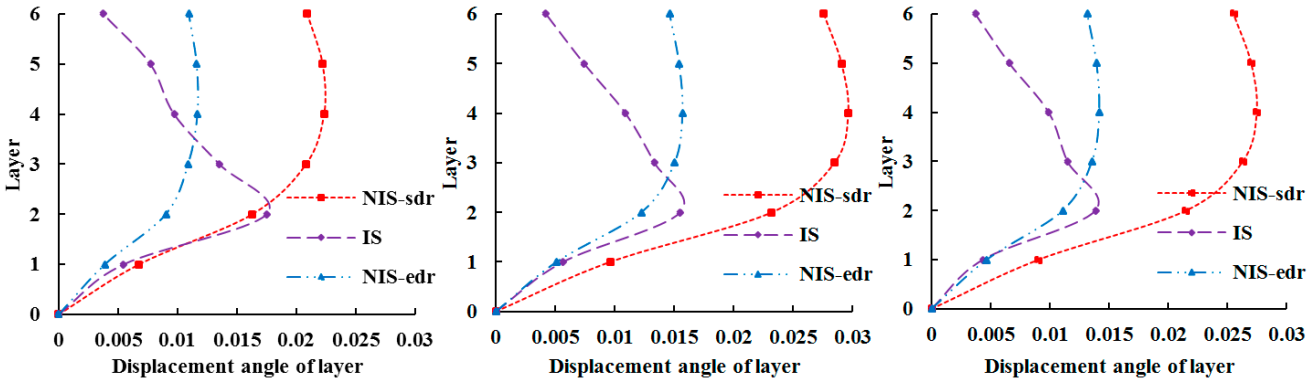


Figure 16. Each structural layer's maximum displacement. (**a**) Transverse EL-Centro wave; (**b**) Transverse Taft wave; (**c**) Transverse artificial wave.

4.4.4. Displacement Angle of Each Layer of Structure

Because container floors use channel steel as a bottom beam, and are covered with wood panel or concrete panel, in the analysis of the multi-layer container structure, due to the container lock being used between the containers, the container bottom of each layer and the container top of the next layer can be considered as having infinite in-plane stiffness. The maximum displacement angle of the layers under different seismic waves is shown in Figure 17.

According to Figure 17, the maximum layer displacement angle of IS and NIS-edr is far less than that of NIS-sdr. At the same time, the maximum layer displacement angle of NIS-edr and NIS-sdr mainly occurs in the upper part of the structure, and the maximum layer displacement angle of IS occurs in the second layer of the structure. The maximum layer displacement angles of the three structures under three seismic waves are shown in Table 10.



(**a**) (**b**) (**c**)

Figure 17. Each structural layer's displacement angle. (**a**) Transverse EL-Centro wave; (**b**) Transverse Taft wave; (**c**) Transverse artificial wave.

Table 10. The structural maximum displacement angles under different seismic waves.

Structure Type	Maximum Displacement Angle		
	EL-Centro Wave	Taft Wave	Artificial Wave
NIS-sdr	1/45	1/38	1/36
NIS-edr	1/85	1/64	1/71
IS	1/58	1/65	1/72

According to the literature [45], the elastic-plastic layer displacement angle limit value is 1/50 of a high-rise steel structure. According to Table 10, the maximum layer displacement angle of NIS-sdr is far more than the standard specified value of 1/50 under the three seismic waves, and cannot meet the requirements. The maximum layer displacement angle of NIS-edr is reduced and is less than the standard specified value of 1/50 under the three seismic waves. At the same time, for the IS, the layer displacement angle is also less than the standard specified value. This shows that the IS is effective for the container structure to resist earthquakes.

By comparing the calculation results of NIS-edr and IS, the maximum layer displacement angles of the two types of container structures are almost the same under the Taft and artificial waves. This shows that an equivalent damping ratio formula can be used in the calculation of IS.

4.4.5. Displacement of Each Layer of Structure

Under the three kinds of seismic waves, the displacement of each layer with the change in time of IS is shown in Figure 18. As can be seen from Figure 18, the slip of each layer of IS is not the same. The slip of the upper part of the structure is larger than the bottom part, and the slip under the Taft wave is the largest, which shows that the spectrum of the seismic wave will obviously affect the structural dynamic response. As can be seen from Figure 18b, the maximum slip of the sixth layer of the structure under the three seismic waves can reach 30 mm. So when the IS is set up, the length of the sliding hole on the corner fitting is set to 35 mm to meet the requirements.

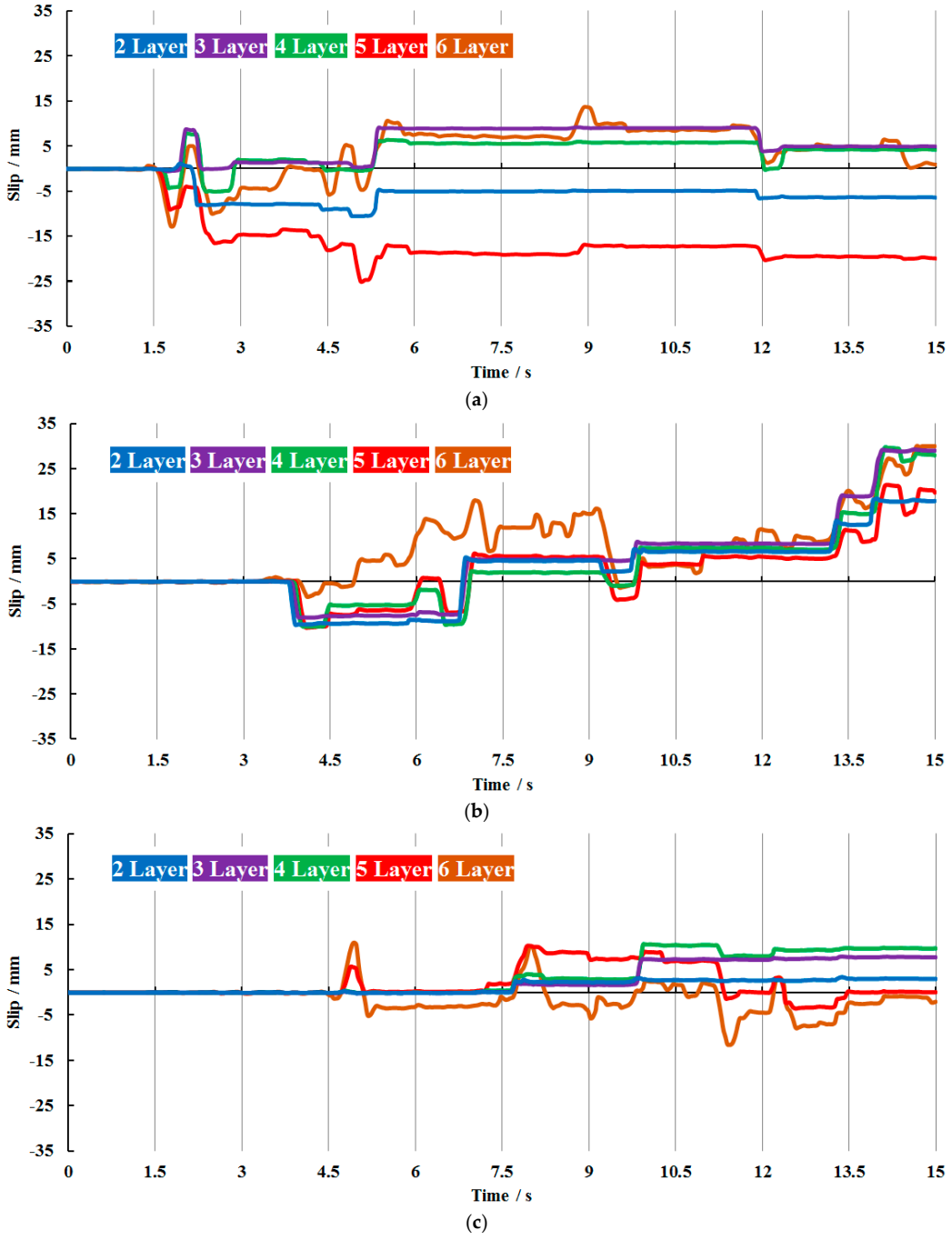


Figure 18. Slip of each layer of IS. (**a**) Transverse EL-Centro wave; (**b**) Transverse Taft wave; (**c**) Transverse artificial wave.

4.4.6. Energy Dissipation Capacity of the IS

To quantify the energy dissipation capacity of the IS, the hysteresis curves (shear force versus inter-story displacement) of the second layer—where the maximum inter-story displacement occurs—are extracted from the nonlinear time-history analysis. Figure 19 presents the hysteresis loops of the IS under the three seismic waves.

The hysteresis loops exhibit a characteristic rectangular shape typical of Coulomb friction damping. The area enclosed by each loop represents the frictional energy dissipated per cycle. Under the Taft wave, which induced the largest inter-story slip, the hysteresis loops are widest, indicating the greatest energy dissipation per cycle. The EL-Centro wave, with its higher frequency content, produces narrower loops but more cycles of energy dissipation. The artificial wave, which matches the target design spectrum, yields an intermediate response.

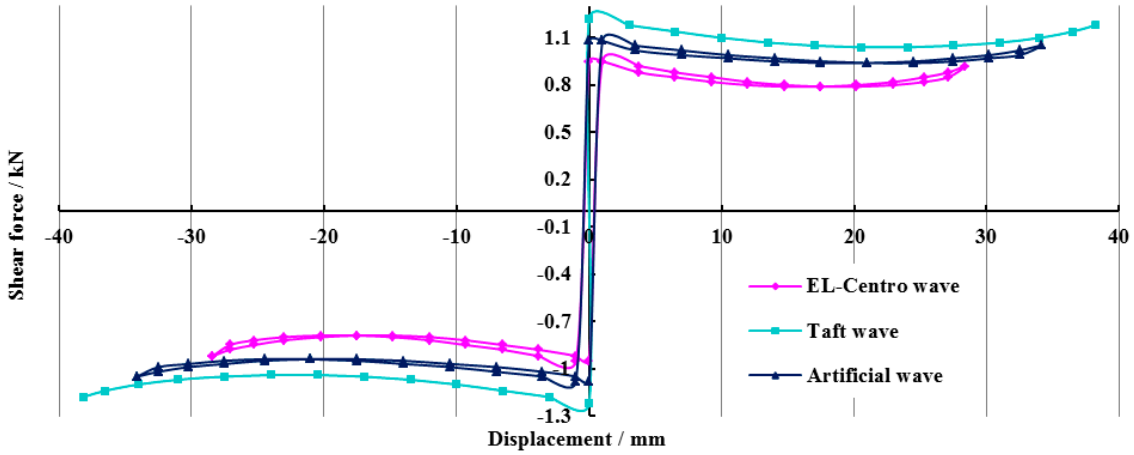


Figure 19. Hysteresis loops of IS.

Table 11 summarizes the total dissipated energy over the entire 15 s duration of seismic excitation for each wave, along with the corresponding peak inter-story drift at the second layer. The IS dissipates substantial seismic energy through friction at the sliding interfaces: 42.6 kJ under the EL-Centro wave, 67.8 kJ under the Taft wave, and 58.3 kJ under the artificial wave. The Taft wave, producing the largest drift, also results in the highest energy dissipation. The dissipated energy is calculated as the cumulative area enclosed by the hysteresis loops at the second layer over the 15 s excitation duration. Peak inter-story drift is taken from the same layer.

Table 11. Energy dissipation and peak drift of the IS under different seismic waves.

Seismic Wave	Total Dissipated Energy/kJ	Peak Inter-Story Drift/mm	Peak Drift Ratio
EL-Centro wave	42.6	28.4	1/58
Taft wave	67.8	38.2	1/65
Artificial wave	58.3	34.1	1/72

Furthermore, the cumulative dissipated energy over time is shown in Figure 20. The energy dissipation rate is highest during the strong-motion phase of each seismic wave (approximately 2–10 s), after which it gradually stabilizes as the structural vibrations attenuate.

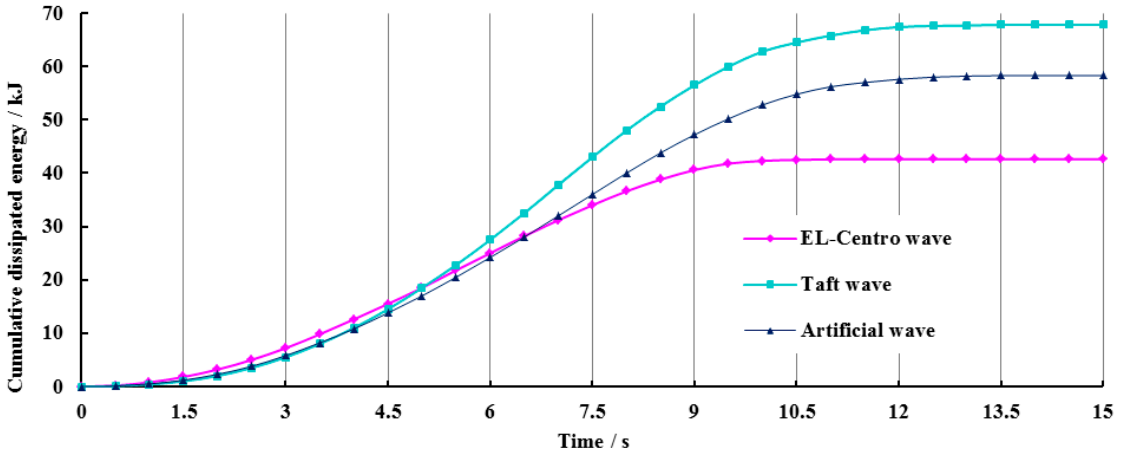


Figure 20. Cumulative dissipated energy of IS.

5. Conclusions

This study proposes IS for multi-story modular container buildings, which utilizes friction energy dissipation between container corner pieces to mitigate seismic response. The novelty of the proposed IS lies in its passive, low-cost, and easily implementable mechanism that does not require additional damping devices. Unlike conventional seismic isolation approaches such as lead rubber bearings or shape memory alloy connections, which often require specialized materials and complex installation, the IS leverages the existing corner fitting connections—a standardized component already present in all container buildings—by introducing slotted holes that permit controlled sliding. This makes the IS particularly suitable for modular container construction, where cost-effectiveness, construction speed, and simplicity are essential.

5.1. Summary of Key Findings

Based on experimental stiffness tests, theoretical random vibration analysis, and nonlinear finite element time-history simulations under strong earthquake excitations (EL-Centro wave, Taft wave, and artificial wave), the following conclusions are drawn:

(1) Container stiffness characteristics. Lateral stiffness tests on 20C, 40C, and 20CC yielded stiffness values of 58.07 kN/mm, 33.41 kN/mm, and 60.03 kN/mm, respectively. The stiffness of 20C is greater than that of 40C due to the increased deformation of longer containers. For 20CC, the stiffness is only marginally higher than that of a single 20 ft container because the limited axial stiffness of the top beam restricts load transfer to the second container.

(2) Equivalent damping formulation. Using the linear equivalent method and random vibration theory, the relationship between the equivalent damping ratio of each structural layer and the inter-layer friction coefficient was derived. For the six-story container building with μ = 0.15, the equivalent damping ratios from the second to sixth layers were calculated as 0.090, 0.089, 0.088, 0.087, and 0.084 (using 20 ft containers), respectively, with an overall equivalent damping ratio of 0.081 for the IS.

(3) Seismic response reduction. Compared to the NIS-sdr and NIS-edr, the proposed IS significantly reduces the maximum inter-story displacement and inter-story drift ratio. Under the Taft wave, the maximum displacement angle of IS (1/65) is substantially smaller than that of NIS-sdr (1/38) and comparable to NIS-edr (1/64). The maximum displacement angle of IS under all three seismic waves satisfies the 1/50 limit specified in steel structures, whereas NIS-sdr violates this limit.

(4) Effect of seismic wave characteristics. The spectral characteristics of seismic waves significantly influence the dynamic response of the IS. The Taft wave, which has a broader frequency band and multi-peak characteristics, induced the largest inter-story slip (up to 30 mm at the sixth layer). Based on this observation, the sliding hole length on the corner fitting is recommended to be 35 mm to accommodate the maximum slip under rare earthquakes while maintaining structural integrity.

5.2. Practical Engineering Implications

The following practical recommendations are made for engineers designing seismic-resistant modular container buildings:

(1) Adopt a friction coefficient of μ = 0.15 for sliding interfaces. This value ensures that under rare earthquakes (e.g., 9-degree fortification, PGA = 0.4 g), the inertial forces overcome static friction and initiate sliding, allowing friction energy dissipation. Under frequent earthquakes, the structure remains locked and behaves as a conventional non-isolated system. The friction surface should be manufactured with a roughness of 0.8–1.6 μm to maintain stable kinetic friction.

(2) Set the slotted hole length on corner fittings to 35 mm. Based on time-history analyses under the Taft wave—which produced the largest inter-story slip—the maximum slip observed at the sixth layer was 30 mm. A 35 mm slot length provides a 5 mm safety margin, preventing collision or dislodgment while accommodating expected displacements under rare seismic events.

(3) Prefer 20 ft containers over 40 ft containers for multi-story construction. Lateral stiffness tests show that a single 20 ft container provides 58.07 kN/mm, which is 74% higher than that of a 40 ft container (33.41 kN/mm). Higher stiffness reduces inter-story drift and the whipping effect in taller structures. If longer spans are necessary, 20CC offers only marginal stiffness improvement (60.03 kN/mm) and is less efficient than using individual 20 ft units.

(4) Perform nonlinear time-history analysis with at least three seismic waves. The study demonstrates that seismic wave characteristics significantly influence IS performance. For example, under the same PGA (620 cm/s^2), the Taft wave induced a maximum slip of 30 mm, while the EL-Centro wave produced much smaller displacements. It is recommended to use EL-Centro, Taft, and a site-matched artificial wave to capture a wide range of frequency contents and ensure robust design.

(5) Install sliding isolation devices at every inter-layer interface. Analysis shows that slip displacements are not uniform across height: upper layers (e.g., 5th and 6th floors) experience larger slips than lower ones. Therefore, sliding interfaces should be provided between every adjacent layer—not only at the base. Special attention should be given to corner fitting connections and sliding hole alignment during construction to ensure free movement under strong earthquakes.

5.3. Limitations and Future Research Directions

Despite the promising results, this study has several limitations that should be addressed in future work:

(1) Experimental validation. The present study is based on finite element simulations and theoretical analysis. Full-scale shake table tests on multi-story container buildings with IS are necessary to validate numerical predictions and capture potential second-order effects (e.g., overturning, P-Δ effects) that were not considered in the current model.

(2) Multi-directional seismic loading. Only horizontal seismic excitations were considered. In reality, earthquakes impose multi-directional (horizontal and vertical) ground motions. The vertical component may affect the normal force at the friction interface, thereby influencing the sliding behavior. Future studies should investigate the IS performance under bi-directional and tri-directional seismic loading.

(3) Optimization of the friction coefficient. It should be acknowledged that the proposed equivalent damping Equation (35) is derived under the continuous sliding assumption (5). This assumption is valid only when the friction coefficient μ satisfies Equation (1).

(4) Stick-slip behavior under weak earthquakes. For higher friction coefficients or lower seismic intensities, the structure may exhibit stick-slip or non-sliding behavior, and the applicability of Equation (35) requires further verification. Therefore, the analytical results presented herein are primarily applicable to moderate-to-strong seismic excitations with relatively low inter-story friction coefficients.

(5) Long-term durability and maintenance. The effects of corrosion, wear, and repeated sliding on the friction coefficient and the sliding hole geometry should be investigated to ensure the long-term reliability of the IS over the building's service life.

Author Contributions: Conceptualization, X.Z.; methodology, Y.Z.; software, Y.Z.; validation, Y.Z.; formal analysis, Y.Z.; data curation, Y.Z.; writing—original draft preparation, Y.Z.; project administration, X.Z. All authors have read and agreed to the published version of the manuscript.

Funding: This research was funded by the National Natural Science Foundation of China, grant number: 52178275.

Data Availability Statement: The original contributions presented in this study are included in the article. Further inquiries can be directed to the corresponding author.

Conflicts of Interest: The authors declare no conflict of interest.

Abbreviations

IS	The sliding friction isolation system
c_{ei}	The equivalent damping of *i* layer of structure (N·s/m)
μ	The friction coefficient of inter layer
NIS-sdr	The non-isolation system with standard damping ratios
NIS-edr	The non-isolation system with equivalent damping ratio
l	The dimension in the length direction of the container (6058 mm)
h	The dimension in the height direction of the component (2591 mm)
w	The dimension in the width direction of the component (2438 mm)
t	The thickness of specimen material (mm)
E	The modulus of elasticity (10^5 MPa)
P	The Poisson's ratio
σ_y	The yield strength (MPa)
σ_b	The ultimate strength (MPa)
20C	20 ft container
40C	40 ft container
20CC	connected 20 ft container
LE	The loading end of stiffness test for container
NLE	The non-loading end of stiffness test for container
F	The load on a single-sided container (kN)
F_{max}	The maximum load on a single-sided container (kN)
l	The number of load levels
Δ_{LE}	The loading end displacement (mm)
Δ_{NLE}	The non-loading end displacement (mm)
k	The single side container stiffness (kN/mm)
$2k$	The container stiffness (kN/mm)
c	The container damping (N·s/m)
m	The container mass (kg)
i, j	The number
g	The gravity acceleration (m/s^2)
x	The displacement of each layer container to the ground (mm)
$\boldsymbol{M}$	The structure mass matrix
$\boldsymbol{C}$	The structure damping matrix
$\boldsymbol{K}$	The structure stiffness matrix
$\boldsymbol{F_f}$	The friction matrix between containers of each layer
$\boldsymbol{I}$	The identity matrix
sgn(x)	The symbolic function
e_i	The error generated by the linear equivalent of *i* layer of structure
$\sigma_{\dot{u}_i}$	The mean square deviation of $\dot{u}_i$
ς_{ei}	The equivalent damping ratio of *i* layer of structure
ζ	The damping ratio
ω	The self-vibration frequency (rad/s)
S_0	The spectral density constant of white noise (m^2/s^3)

e(t)	The envelope function
W(t)	The steady process of white noise (m/s^2)
< >	The overall mean
$\delta(\tau)$	The dirac function
O	The origin coordinates
σ	The stress coordinate axis
ε	The strain coordinate axis
ε_y	The yield strain
hc	The dimension in the height direction of the component (mm)
lc	The dimension in the length direction of the component (mm)
wc	The dimension in the width direction of the component (mm)
E	The experiment method
FEM	The finite element method
E_{EFEM}	The error between experiment and finite element method (%)
T	The period (s)
α, β	The constant
ξ_{eq}	The equivalent damping ratio of the overall structure
ξ_{eqj}	The equivalent damping ratio of the j isolation layer structure
K_j	The horizontal stiffness of the j isolation layer structure

References

1. Zuo, Y. Theoretical Simulated and Experimental Research on Resistant Lateral Stiffness of Container Structure. Ph.D. Thesis, Harbin Institute of Technology, Harbin, China, 2016.
2. Sibylle, K. *Prefab & Modular Housing: Back Again and Better Than Ever*; Braun: Salenstein, Switzerland, 2026.
3. Wei, Q.; Ding, Y. *Regeneration of Container Building Space*; China Architecture & Building Press: Beijing, China, 2025.
4. Gu, Q. *The Localization Application Strategy of Modular Architectural Design*; China Architecture & Building Press: Beijing, China, 2022.
5. Zha, X.X.; Zuo, Y.; Chen, S.Y. Study on the optimal design of the members of contaniner building with building materials i: Side board optimization. In Proceedings of the 2013 2nd International Conference on Civil Engineering and Material Engineering, Wuhan, China, 10 September 2014.
6. Zha, X.X.; Zuo, Y.; Chen, S.Y. Study on the optimal design of the members of contaniner building with building materials ii: Joint and corner column optimization. In Proceedings of the 2013 2nd International Conference on Civil Engineering and Material Engineering, Wuhan, China, 10 September 2014.
7. David, W. *The Future of Modular Architecture*; Routledge: Oxfordshire, UK, 2021.
8. Avi, F. *Pre-Fab Living*; Thames & Hudson: London, UK, 2021.
9. Terence, L. *Shipping Container Homes*; New Communication Line Com: West Chester, PA, USA, 2024.
10. Cheng, Y. *Recent Trends in Cold-Formed Steel Construction*; Woodhead Publishing: Cambridge, UK, 2024.
11. *T/CECS 1932-2025*; Standard for Quality Acceptance of Container Houses. China Planning Press: Beijing, China, 2025.
12. Liang, W.; Ye, X.; Zhou, Y.; Nie, C.; Xing, J.; Liu, L.; Zhu, J.; Zhang, J.; Miao, L. The thermal performance of a typical prefab container house. *Case Stud. Therm. Eng.* **2024**, *64*, 105445. [CrossRef]
13. *T/CECS 1716-2024*; Technical Specification for Modular Building of Temporary Camps. China Planning Press: Beijing, China, 2024.
14. *T/CECS 1125-2022*; Technical Specification for Modular Emergency Infectious Diseases Hospital. China Planning Press: Beijing, China, 2022.
15. *T/CABEE 074-2024*; Technical Standard for Modular Pressurized Buildings in High-Altitude Areas. China Architecture & Building Press: Beijing, China, 2024.
16. Zha, X.; Zuo, Y. Finite element study of container structure under normal and high temperature. *Math. Probl. Eng.* **2016**, *2016*, 235. [CrossRef]
17. Zha, X.; Zuo, Y. Theoretical and experimental studies on in-plane stiffness of integrated container structure. *Adv. Mech. Eng.* **2016**, *8*, 345. [CrossRef]
18. Zha, X.; Zuo, Y. Theoretical and experimental studies on in-plane stiffness of container structure with holes. *Adv. Mech. Eng.* **2018**, *8*, 246. [CrossRef]
19. Corfar, D.A.; Tsavdaridis, K.D. A hybrid inter-module connection for steel modular building systems with SMA and high-damping rubber components. *Eng. Struct.* **2023**, *289*, 116281. [CrossRef]
20. Zixiao, W.; Daniel, T.K. Optimality criteria-based minimum-weight design method for modular building systems subjected to generalised stiffness constraints: A comparative study. *Eng. Struct.* **2022**, *251*, 113472.

21. Lyu, Y.F.; Li, G.Q.; Cao, K.; Zhai, S.Y.; Wang, Y.B.; Mao, L.; Ran, M.M. Bending behavior of splice connection for corner-supported steel modular buildings. *Eng. Struct.* **2022**, *250*, 113460. [CrossRef]
22. Lyu, Y.F.; Li, G.Q.; Cao, K.; Zhai, S.Y.; Li, H.; Chen, C.; Wang, Y.Z. of splice connection during transfer of vertical load in full-scale corner-supported modular building. *Eng. Struct.* **2021**, *230*, 111698. [CrossRef]
23. Liew, R.; Chua, Y.S. Innovative modular systems for high-rise buildings. *Eng. Struct.* **2025**, *323*, 119270. [CrossRef]
24. Pejman, S.; Babak, A.; Kamyar, K. Novel rocking interconnection for superior prefabricated prefinished modular building system. *Eng. Struct.* **2025**, *343*, 120934. [CrossRef]
25. Zhang, Y.; Sun, T.; Liu, J.; Wang, H.; Liu, Z.; Yang, B.; Chen, K. Progressive collapse behavior of a beam–column substructure of a modular steel building under an interior cluster-column loss scenario. *J. Struct. Eng.* **2025**, *151*, 4025111. [CrossRef]
26. Lacey, A.W.; Chen, W.; Hao, H.; Bi, K. Lateral behaviour of modular steel building with simplified models of new inter-module connections. *Eng. Struct.* **2021**, *236*, 112103. [CrossRef]
27. Zhang, J.Z.; Deng, Y.T.; Li, G.Q.; Cao, K.; Chen, X.; Yu, Z.W. Collapse performance of steel modular building under corner module loss: Full-scale test and analysis. *Eng. Struct.* **2025**, *337*, 120360. [CrossRef]
28. Zha, X.X.; Zuo, Y.; Liu, L.; Wang, X.J. Analysis of mechanical properties of container structure under earthquake action. *J. South China Univ. Technol. (Nat. Sci. Ed.)* **2015**, *43*, 92–98.
29. Zha, X.; Zuo, Y.; Liu, L. Theoretical and finite element study on longitudinal stiffness of multi-body container building. *Prog. Steel Build. Struct.* **2014**, *16*, 24.
30. Mo, Z.; Lai, B.; Shu, G.; Yang, T.Y.; Ventura, C.E.; Liew, J.R. Enhancing seismic resilience in modular steel building through three-dimensional isolation. *Eng. Struct.* **2025**, *323*, 119269. [CrossRef]
31. Mo, Z.; Lai, B.; Shu, G.; Chen, P.; Yang, T.Y. Performance-based seismic design method of stacked modular steel building based on three-dimensional seismic isolation. *Eng. Struct.* **2025**, *336*, 120438. [CrossRef]
32. Di, W.; Baian, L.; Yan, X. Seismic performance of modular steel structure with X-shaped rubber bearings: Shaking table tests. *Adv. Struct. Eng.* **2025**, *28*, 1461–1475.
33. Emamikoupaei, A.; Tsavdaridis, K.D.; Bigdeli, A.; Saffarzadeh, K. Fragility-based robustness assessment of steel modular building systems: Connection and building height. *J. Constr. Steel Res.* **2025**, *226*, 109199. [CrossRef]
34. *ISO 6892-1:2019*; Metallic Materials-Tensile Testing-Part 1: Method of Test at Room Temperature. International Organization for Standardization: Geneva, Switzerland, 2019.
35. *ISO 668:2020*; Series 1 Freight Continers-Classification, Dimensions and Ratings. International Organization for Standardization: Geneva, Switzerland, 2020.
36. *ISO 1496-1:2013*; Series 1 Freight Containers-Specification and Testing-Part 1: General Cargo Containers for General Purposes. International Organization for Standardization: Geneva, Switzerland, 2013.
37. Zuo, Y.; Zha, X. Fem and experimental study on mechanical property of integrated container building. *Int. J. Steel Struct.* **2018**, *18*, 699–718. [CrossRef]
38. Zuo, Y.; Zha, X. Fem and experimental study on mechanical property of container building with holes. *Int. J. Steel Struct.* **2017**, *17*, 175–194. [CrossRef]
39. *CECS 334: 2013*; Technical Specification for Modular Freight Container Building. China Planning Press: Beijing, China, 2013.
40. Zuo, Y.; Zha, X. Analysis of longitudinal stiffness of container building structure with holes. *J. Tianjin Univ. (Sci. Technol.)* **2015**, *48*, 167–176.
41. *T/CECS 507-2018*; Technical Specification for Steel Modular Buildings. China Planning Press: Beijing, China, 2018.
42. *JGJ/T 466-2019*; Technical Standard for Light Steel Modular Building. China Architecture & Building Press: Beijing, China, 2019.
43. *T/CECS 1575-2024*; Technical Specification for Application of Glass-Fiber Reinforced Plate-Type Modular Buildings. China Architecture & Building Press: Beijing, China, 2024.
44. Ou, J.; Wang, G. *Random Vibration of Structures*; Higher Education Press: Beijing, China, 1998.
45. *GB50011-2010*; Code for Seismic Design of Buildings. China Architecture Industry Press: Beijing, China, 2010.
46. Wang, Y. *Abaqus/cae Analysis User's Guide*; China Machine Press: Beijing, China, 2025.
47. Zuo, Y.; Zha, X. Study on the mechanical properties of stiffening members on the container structure with holes. *Structures* **2025**, *81*, 110161. [CrossRef]
48. Fu, Z.; He, J. *Modal Analysis*; Butterworth-Heinemann: Oxford, UK, 2001.
49. Lago, A.; Trabucco, D.; Wood, A. *Damping Technologies for Tall Buildings Theory, Design Guidance and Case Studies*; Butterworth-Heinemann: Oxford, UK, 2018.

Disclaimer/Publisher's Note: The statements, opinions and data contained in all publications are solely those of the individual author(s) and contributor(s) and not of MDPI and/or the editor(s). MDPI and/or the editor(s) disclaim responsibility for any injury to people or property resulting from any ideas, methods, instructions or products referred to in the content.